



Study on necking defects, microstructure and mechanical properties of TC4 alloy by cross wedge rolling

Peiai Li¹ · Baoyu Wang^{1,2} · Cuiping Yang^{1,2} · Huibo Zhang¹ · Wei Li¹ · Jing Zhou¹

Received: 28 March 2022 / Accepted: 16 September 2022 / Published online: 18 October 2022
© The Author(s), under exclusive licence to Springer-Verlag France SAS, part of Springer Nature 2022

Abstract

The TC4 alloy is an ideal material for the lower control arm of military vehicles due to its low density and high strength. The TC4 alloy lower control arm formed by cross wedge rolling (CWR) has high innovation and application value. Based on the Arrhenius equation, the constitutive equation for the $\alpha + \beta$ two-phase region of the TC4 alloy was established and applied to the finite element model (FEM). The effect of process parameters on the necking defects of TC4 alloy shaft parts formed by CWR was studied and verified by experiments. Additionally, the effects of process parameters on the microstructure and mechanical properties were investigated. The results showed that the softening effect of TC4 alloy makes the rolled workpiece prone to necking defects. Different forming and stretching angles changed the axial forces between the die and the workpiece and affected the relative diameter reduction (RDR) of TC4 alloy rolled parts. The axial force and contact area F_2 between the die and the rolled workpiece increase with the increase in the area reduction, which further has a significant effect on the RDR. The increase in deformation temperature causes the metal to flow less in the axial direction and more in the circumferential direction, and thus reduces the RDR. Moreover, deformation temperature and area reduction have a significant effect on the volume fraction of the primary α phase (f_{α_e}), the morphology and mechanical properties of the α phase. The strength properties of TC4 alloy can be improved by interleaving equiaxed α phase with disordered secondary α phase and increasing the f_{α_e} . The grain refinement and strength properties can be improved by increasing the area reduction to more than 30%.

Keywords Cross wedge rolling · TC4 alloy · Necking defect · Microstructure · Mechanical properties

Introduction

Ti-6Al-4 V (TC4) is an ideal material for the aerospace and military industry due to its lightweight and high strength [1, 2]. The use of TC4 alloy in the lower control arm of the wheeled armored vehicle not only reduces the weight of the vehicle but also improves the bearing capacity of the

suspension. The lower control arm of the vehicle should meet the mechanical performance requirements of ultimate tensile strength ≥ 940 MPa, yield strength ≥ 860 MPa and elongation $\geq 13\%$. The traditional manufacturing process of vehicle lower control arm is shown in Fig. 1. Eccentricity, bending or crack defects are easy to occur when the shaft parts of the lower control arm are produced by the free forging process, and the forging force required is also relatively high. The precision forging process has the disadvantage of expensive equipment and is not suitable for the production of large quantities of parts [3–5]. Compared to traditional processes, CWR process has unique advantages in the processing of shaft parts, not only in terms of improving the forming accuracy of the parts, saving material and energy, but also in terms of reducing the processing cost. In addition, the production efficiency can be increased during the manufacture of shaft parts which can meet the requirements of modern manufacturing [6].

In the CWR process, appropriate die parameters and rolling process parameters can be selected to control the

✉ Baoyu Wang
bywang@ustb.edu.cn

✉ Cuiping Yang
yangcp@me.ustb.edu.cn

Peiai Li
beibeipepei@126.com

¹ School of Mechanical Engineering, University of Science and Technology, No.30 Xueyuan Road, BeijingHaidian District 100083, Beijing, China

² Beijing Laboratory of Metallic Materials and Processing for Modern Transportation, Beijing 100083, China

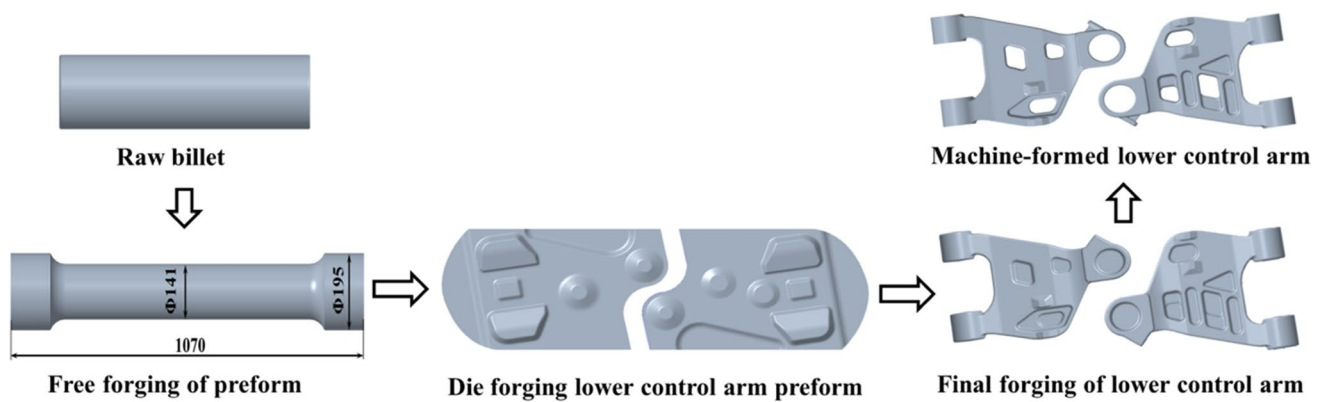


Fig. 1 The traditional manufacturing process of vehicle lower control arm

forming quality of steel parts [7, 8]. The surface quality of the TC4 alloy preforms has a very significant influence on the forming quality of the final forgings. Therefore, it is also necessary to select reasonable process parameters and die parameters to effectively control the surface quality. Li et al. [9] explained the defects in the three types of rolling processes: improperly formed workpiece cross-section (excess slip), surface defects (spiral grooves, necking, overlapping) and internal defects (center cracking), which mainly appeared in the CWR process. He also pointed out that necking defects are more likely to occur in the case of large area reduction (70%). The research on necking of steel rolled part is mainly focused on the condition of area reduction $> 70\%$, and it is not easy to produce necking when the area reduction is $< 35\%$ [10]. Zhou et al. [11] established a twice-stage CWR model of connecting rod preform by using the rigid-plastic finite element method. The necking law of twice-stage CWR was analyzed by the distribution law of area reduction coefficient. It was found that the necking is the minimum when the area reduction distribution coefficient is close to 1. At the same time, the change laws of effective strain, displacement and damage were analyzed. Based on the finite element method, Pater et al. [12] developed the three-dimensional mechanical model of the CWR process. The uncontrolled slipping and core necking in the rolling process were predicted. Li et al. [13] investigated the effect of CWR rolling parameters on the formability of TC4 alloy. The results showed that the axial force of rolling increased with increasing die forming angle, contributing to necking defects in the rolled parts. Variations in the stretching angle did not have a significant effect on necking defects. At an area reduction of 72.4% and deformation temperatures of 850 °C and 950 °C, respectively, the rolled parts showed serious necking defects. When the deformation temperature was increased to 1020 °C, only slight necking occurred due to the increase in plastic elongation at high temperature.

When forming TC4 alloy using the CWR process, the rolled parts should not only have high forming accuracy but also have good mechanical properties, so that the formed parts can meet the application requirements. Microstructure characteristics affect the mechanical properties of $\alpha + \beta$ phase alloy, especially the content and morphology of the primary α phase [14]. The size, morphology and volume fraction of the phases can be regulated by different heat treatment methods and deformation processing parameters. Zhai et al. [15] used a triple heat treatment process to control the α phase content and morphology of the TC4 alloy, and optimized the mechanical properties of the TC4 alloy. The phase composition and morphology are also significantly affected by the thermomechanical processing method and cooling method, and have been extensively studied by many authors [16, 17]. Xu et al. [18] investigated the effect of isothermal forging and subsequent heat treatment on the microstructural evolution of Ti-17 alloys with a lamellar colony structure. It was found that the evolution of the length and thickness of the lamellar α phase was mainly strain and temperature dependent. The evolution of the refinement of lamellar α grains into equiaxed α grains with an average grain size of 1.9 μm was investigated by Zhang et al. [19] using a multidirectional isothermal forging process. The results showed that dynamic recrystallisation was the main cause of grain refinement. The mechanical properties of the forged TC4 alloy were greatly improved both at room temperature and 400 °C. CWR is different from isothermal forging. It is a non-isothermal rolling process. The workpiece undergoes complex radial and axial deformations and temperature changes during the rolling. These changes not only cause changes in the quality of the surface and core of the workpiece at the macro-scale, but also cause changes in the morphology and composition of the phase at the micro-scale [20–22]. The mechanical properties of the workpiece will also change accordingly.

The existing research on necking defects caused by CWR mainly focuses on various steels. Further, the necking laws of titanium alloys have only been briefly explained, while the

mechanisms of necking defects lack more in-depth research. The effect of CWR process on the microstructure evolution of TC4 alloy solid shaft parts and the mechanism of phase composition and morphology on mechanical properties are not very clear. In this paper, the necking defects, microstructure and mechanical properties of TC4 alloy formed by CWR were investigated. Firstly, the flow curves in the $\alpha + \beta$ phase region of TC4 alloy were obtained by isothermal hot compression tests and the corresponding constitutive equation was established and applied to the FEMs. Secondly, the effect of CWR process parameters on the RDR of TC4 alloy shaft parts was investigated by FEM and verified by corresponding CWR experiments. Further, the microstructure evolution and mechanical properties of TC4 alloy shaft parts formed by CWR were investigated.

TC4 alloy material characteristic

Materials and experimental procedure

The microstructure of the as-received TC4 alloy bar is shown in Fig. 2. The microstructure contains equiaxed primary α phase and lamellar secondary α phase, with the β phase distributed on the boundary of the α phase. Table 1 shows the chemical composition of the TC4 alloy used in this experiment. The β -phase transus temperature is 992 °C.

The isothermal compression experiments for TC4 alloy were carried out on the Gleeble-1500D thermo-simulation

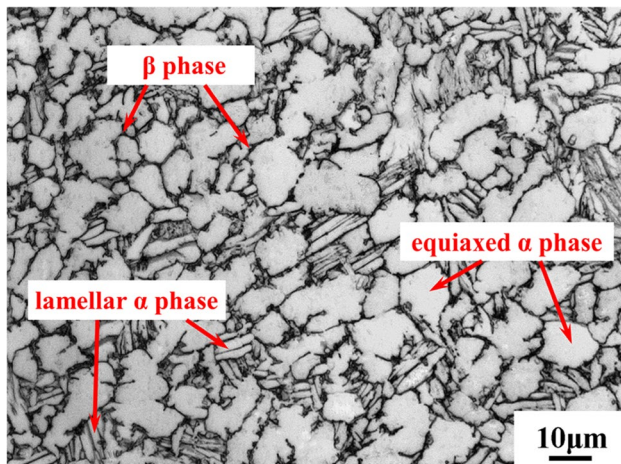


Fig. 2 Optical micrograph of as-received TC4 alloy

Table 1 Chemical composition of TC4 alloy (in Wt%)

Main chemical component			Impurity content						
Ti	Al	V	Fe	C	N	H	O	Si	
Bal	6.41	4.33	0.17	0.007	0.005	0.0016	0.16	0.013	

machine. The deformation temperatures and strain rates were set at 850 °C, 900 °C, 950 °C, and 0.01 s⁻¹, 0.1 s⁻¹, 1 s⁻¹, 10 s⁻¹, respectively. Prior to the tests, the specimens were heated to the deformation temperature and held for 3 min to ensure uniform heat distribution. After the test, the specimens were quenched in water and then rapidly cooled. The true strain–stress curves in isothermal compression were automatically recorded and saved [23].

Flow behavior

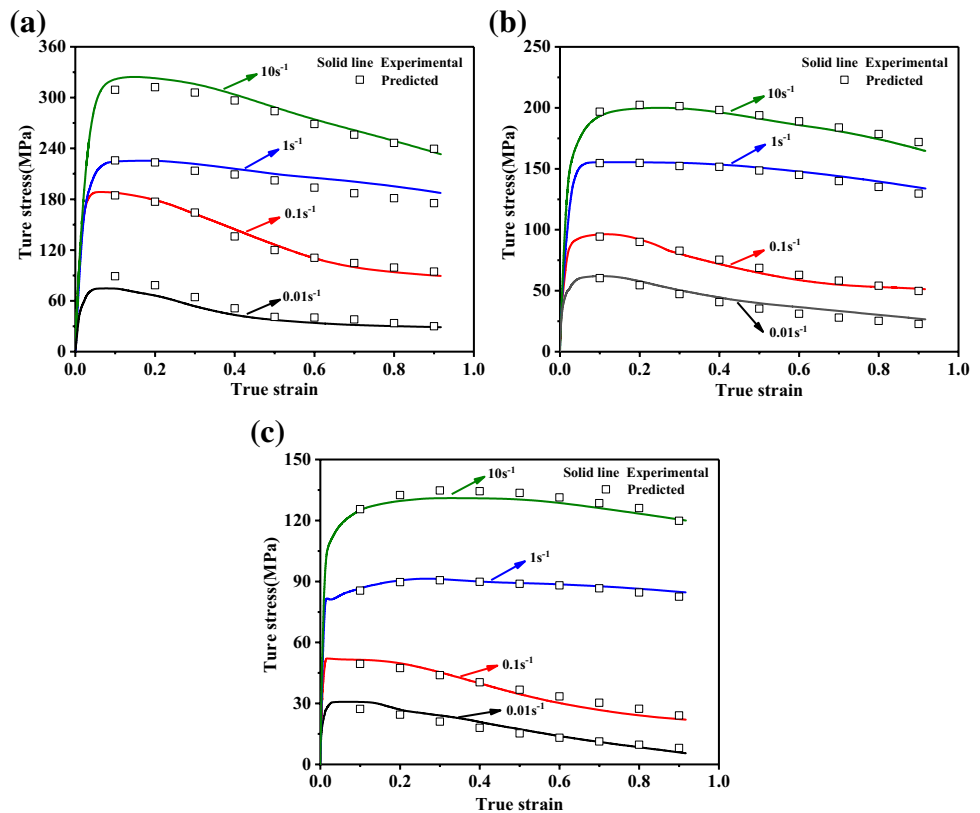
To avoid the β brittleness of TC4 alloy after plastic processing in the β phase region, and ensure that the rolled piece has excellent comprehensive mechanical properties [24]. Therefore, only the CWR process in the $\alpha + \beta$ phase region was investigated in this paper, and the stress–strain equation for the $\alpha + \beta$ phase region was established. The true stress–strain curves for the TC4 alloy are shown in Fig. 3. The trend of the flow stress with temperature and strain rate is reversed. As the deformation temperature increases the value of the flow stress decreases, and as the strain rate increases the value of the flow stress increases. Subject to work hardening, the stress increases sharply and reaches a peak within a very small strain range, then the stress begins to decrease with increasing strain and flow softening occurs. This phenomenon is more pronounced at higher temperatures and lower strain rates. In general, the flow softening behaviour of stress–strain is attributed to different deformation mechanisms. Dynamic recrystallization, dynamic recovery and super plasticity mechanisms all contribute to the flow softening behaviour of titanium alloy materials [25, 26].

Determination and verification of material Constants

The constitutive equation of TC4 alloy at high temperatures can be described by the Arrhenius equation, which has been proved to be feasible [1, 13]. The material constants in the equation can be determined according to the isothermal compression test data at different strain rates and temperatures. Three types of constitutive equations and their parameters are as follows.

$$\dot{\epsilon} = A_1 \sigma^{n_1} \exp\left(-\frac{Q}{RT}\right) \quad \alpha \sigma < 0.8 \quad (1)$$

Fig. 3 True stress–strain curves of TC4 alloy: **a** 850 °C, **b** 900 °C, **c** 950 °C



$$\dot{\epsilon} = A_2 \exp(\beta\sigma) \exp\left(-\frac{Q}{RT}\right) \quad \alpha\sigma < 1.2 \tag{2}$$

$$\dot{\epsilon} = A[\sinh(\alpha\sigma)]^n \exp\left(-\frac{Q}{RT}\right) \quad \text{for all } \sigma \tag{3}$$

The Zener–Holloman parameter (Z) is related to the strain rate and temperature, and this parameter has an obvious influence on the deformation behavior of the alloy. It is expressed as follows:

$$Z = \dot{\epsilon} \exp\left(\frac{Q}{RT}\right) \tag{4}$$

where Q is the activation energy ($J \cdot mol^{-1}$), R is the gas constant of $8.3145 (J \cdot mol^{-1} \cdot K^{-1})$, $\dot{\epsilon}$ is the strain rate (s^{-1}), σ is the flow stress (MPa), T is the absolute temperature (K), while A_1, A_2, A, α, n_1 and n are the material constants, and $\alpha = \beta/n_1$. Through a series of calculations, the material constants were determined according to the stress under different compression test conditions [13].

The variation of the main material constants at different strains is shown in Fig. 4. The material constants α, n, Q and $\ln A$ were fitted using a 5th-order polynomial. Equation (5) is the specific expression of the 5th-order equation. All the correlation coefficients (RR) are above

0.99, which indicates that the fitting is appropriate. The Arrhenius constitutive equation in the $\alpha + \beta$ two-phase region can be obtained by substituting the material constants α, n, Q and $\ln A$ in Eq. (5) into Eq. (3).

$$\begin{cases} \alpha = -0.04116\epsilon^5 + 0.12731\epsilon^4 - 0.1466\epsilon^3 + 0.07924\epsilon^2 - 0.01326\epsilon + 0.0103 \\ Q = 2023.83\epsilon^5 - 6104.24\epsilon^4 + 6630.60\epsilon^3 - 2531.78\epsilon^2 - 323.13\epsilon + 709.28 \\ n = 8.56251\epsilon^5 - 24.485\epsilon^4 + 24.379\epsilon^3 - 7.88045\epsilon^2 - 2.5962\epsilon + 4.02785 \\ \ln A = 218.71\epsilon^5 - 653.47\epsilon^4 + 704.53\epsilon^3 - 269.99\epsilon^2 - 30.115\epsilon + 70.05 \end{cases} \tag{5}$$

Once the evaluation of the material constants has been completed, the constitutive equations relating the flow stresses and Zener-Holloman parameters can be written as Eq. (6) according to Eqs. (3) and (4).

$$\sigma = \frac{1}{\alpha} \ln \left\{ \left(\frac{Z}{A}\right)^{\frac{1}{n}} + \left[\left(\frac{Z}{A}\right)^{\frac{2}{n}} + 1\right]^{\frac{1}{2}} \right\} \tag{6}$$

The constitutive equation will be applied for the finite element (FE) simulation of the TC4 alloy shafts formed via CWR. The accuracy of the constitutive equation was evaluated by the average absolute relative error (AARE) and the correlation coefficient (RR). The specific equations are as follows:

Fig. 4 Relationship between material constants and strain: **a** α - ϵ , **b** Q - ϵ , **c** n - ϵ , **d** $\ln A$ - ϵ

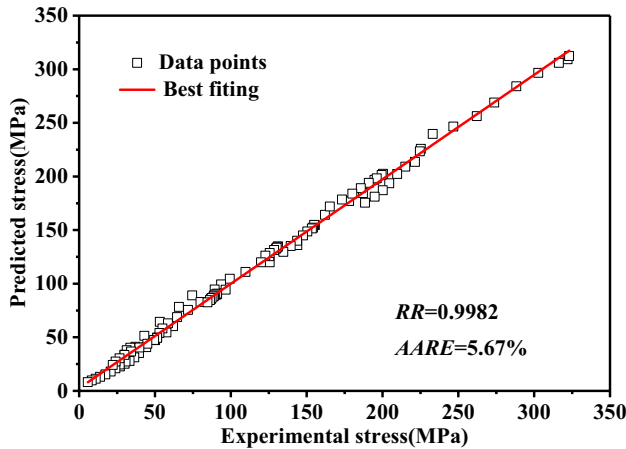
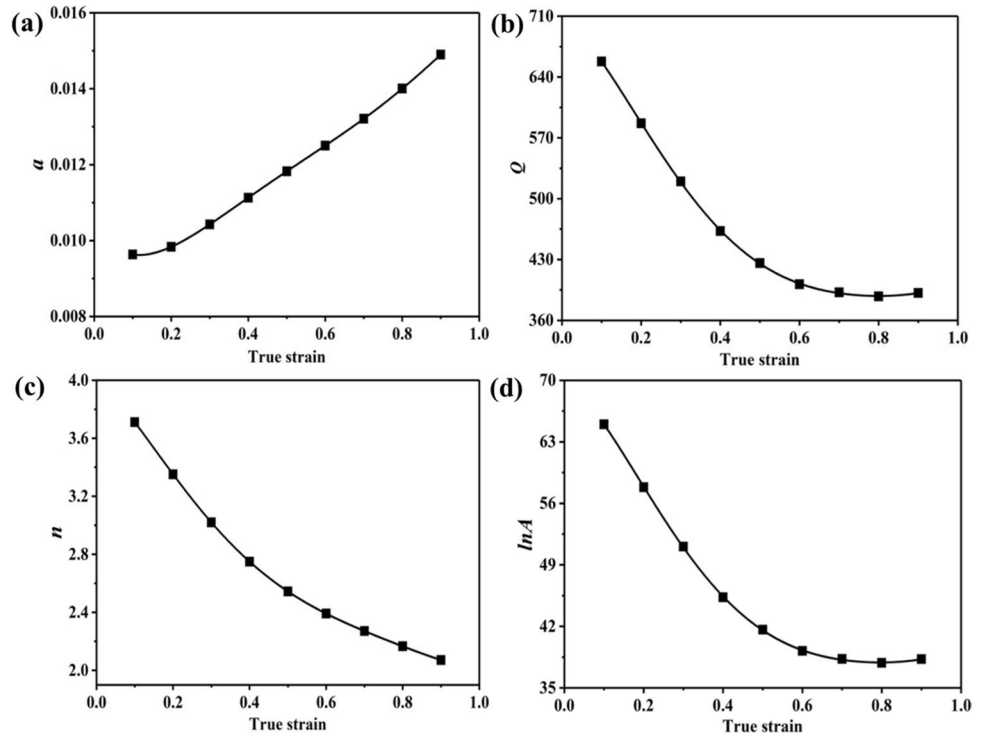


Fig. 5 Comparison of predicted stress and experimental stress

$$RR = \frac{\sum_{i=1}^N (X_i - \bar{X})(Y_i - \bar{Y})}{\sqrt{\sum_{i=1}^N (X_i - \bar{X})^2} \sqrt{\sum_{i=1}^N (Y_i - \bar{Y})^2}} \tag{7}$$

$$AARE = \frac{1}{N} \sum_{i=1}^N \left| \frac{Y_i - X_i}{Y_i} \right| \times 100\% \tag{8}$$

In the Eqs. (7) and (8), X_i and Y_i are the predicted and experimental flow stress, \bar{X} and \bar{Y} are the average predicted and experimental flow stress. It can be seen from Fig. 5 that the RR and $AARE$ values are 0.9982 and 5.67%, respectively.

This shows that the constitutive equation of TC4 alloy established in this paper has high credibility.

Finite element simulation and experiment

Finite element simulation

The FEM diagram of the CWR study and the plan layout parameters of the die are shown in Fig. 6. The FEM of CWR TC4 alloy shaft was established within the FE software of DEFORM-3D. To ensure the accuracy of the geometric size of the model, the number of elements for the workpiece was set to 80,000, and the mesh type was tetrahedral mesh. The rolled workpiece and die in the FEM were set to be symmetrical relative to the center plane. The original diameter of the workpiece is 44 mm. The original lengths of the workpieces with an area reduction of 10%, 30%, 50% and 70% are 135 mm, 120 mm, 110 mm and 90 mm, respectively. The die parameters of the FEM are consistent with the die used for the experiments. The surfaces of the stretching and sizing zones of the die were machined with a gap of 1 mm in depth.

The relevant assumptions and boundary conditions for the FEM were set as follows: (1) The workpiece was set up as a plastic body. (2) The roll dies and guide slats were almost not deformed, so they were set as rigid bodies. (3) The friction factors between the contact surfaces were all constants, including the contact between the die and the rolled workpiece and the contact between the guide slats and the rolled

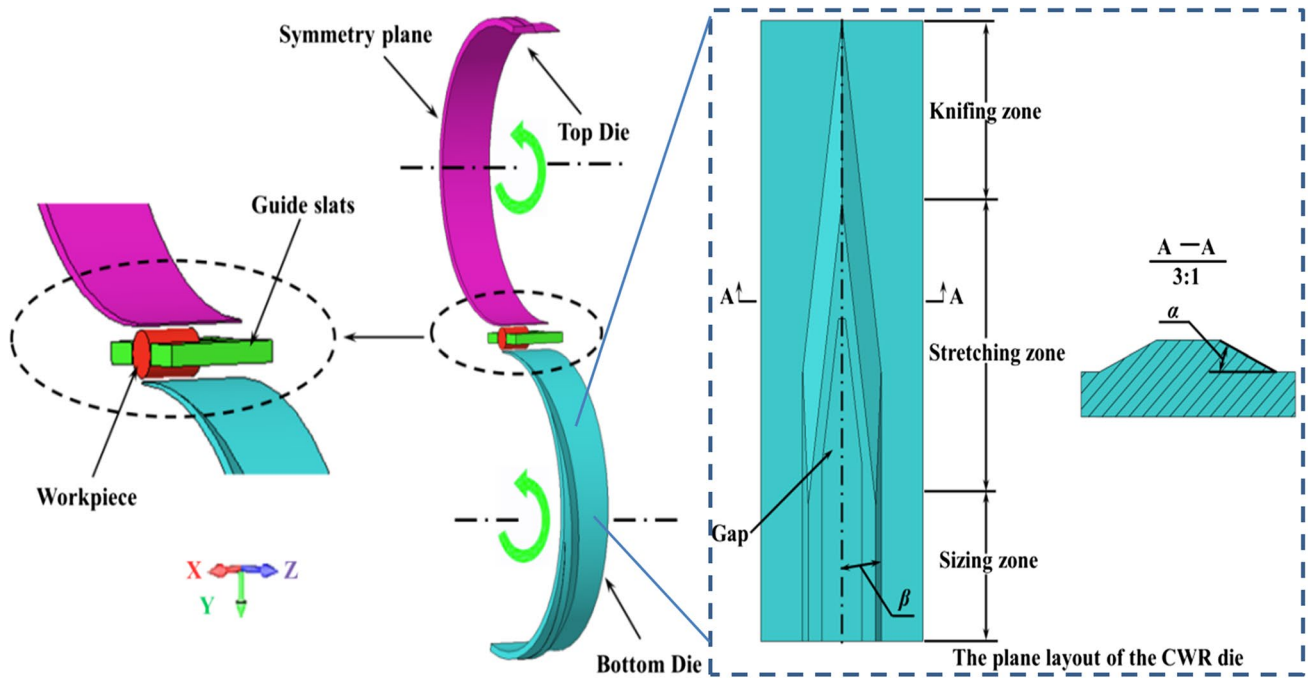


Fig. 6 FEM and die schematic for CWR of TC4 alloy

Table 2 Main parameters of CWR simulation

Parameters	Value
Heat transfer coefficient ($Wm^{-2} K^{-1}$)	11×10^3
Convection coefficient ($Wm^{-2} K^{-1}$)	20
Thermal conductivity ($KWm^{-2} K^{-1}$)	17
Coefficient of mechanical energy to heating	0.9
Friction factor between workpiece and die	0.9
Friction factor between workpiece and guide slats	0.4
Environment temperature ($^{\circ}C$)	20
Temperature of tools ($^{\circ}C$)	20
Speed of roll (rpm)	8

workpiece. The shear friction was selected as the friction type: $f_s = m \times k$, where f_s , m and k are the friction stress, the friction factor and shear yield stress, respectively. (4) The parameters such as heat transfer coefficient and convection coefficient are listed in Table 2. The experimental arrangements are presented in Table 3.

Table 3 The FE simulation and experimental arrangements for CWR of TC4 alloy

Item	Forming angle α ($^{\circ}$)	Stretching angle β ($^{\circ}$)	Area reduction ψ (%)	Deformation temperature T ($^{\circ}C$)
1	30	7.5	50	850,870,890,910
2	30	7.5	10,30,50,70	870
3	30	5,7.5,10	50	870
4	25,30,35	7.5	50	870

Cross wedge rolling experiment

The H630 CWR mill provided by the Beijing University of Science and Technology, which was the experimental equipment used for this experiment, as shown in Fig. 7a. The workpiece was heated in a tube furnace for 45 min before rolling. After heating, the workpiece was quickly transferred to the mill. The workpiece in the process of rolling and the rolled parts are shown in Fig. 7b and c respectively. The rolled parts were water cooled to preserve the complete microstructure.

Microstructure observation and mechanical properties test

The TC4 alloy part was cut into two completely symmetrical parts at the position of the symmetry plane. Then the microstructure of the core, middle and surface regions at the symmetrical section position of the part was observed.

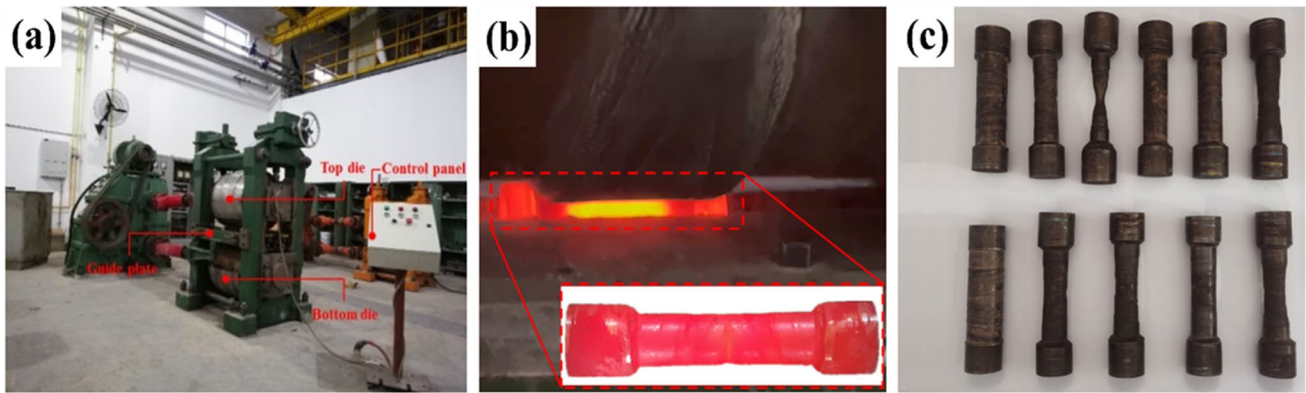


Fig. 7 Experimental equipment and the rolled workpieces: **a** H630 mill, **b** Workpiece being rolled, **c** Rolled parts

The microstructure of the sample was observed by an optical microscope (OM). The OM specimen was obtained by mechanical grinding, polishing and then etching with corrosion agent. The corrosion agent was composed of HF, HNO₃ and H₂O in the ratio of 1:3:7. The geometrical parameters and test methods of the specimens for the room temperature tensile test were carried out according to GB/T228.1–2010.

Results and discussion

Dimensional verification of cross wedge rolling simulation

The comparison between the experimental result and the simulation result of the outline of the rolled part at $\alpha = 7.5^\circ$, $\beta = 30^\circ$, $\psi = 50\%$, and $T = 910^\circ\text{C}$ is shown in Fig. 8. The different colors in the scale represent the radial distance between the FE simulation result and the experimental result at a certain point. These geometric dimensions were compared using Geomagic Qualify software. As shown in Fig. 8a, the maximum and minimum radial deviations are distributed in the range of 0.980 mm to -0.980 mm. As can be seen in Fig. 8b to c, the range of radial deviations for sections P1, P2 and P3 are much smaller. The maximum radial dimensional deviation is only 1.1%. This shows that the FEM used in this paper is reliable.

The RDR is an important indicator to evaluate the necking defects of shaft parts. The following Eq. (9) was used to calculate the RDR:

$$RDR = \frac{D_0 - D_{min_{av}}}{D_0} \quad (9)$$

D_0 and $D_{min_{av}}$ represent the target diameter of the rolled workpiece and the average diameter of the transverse section

with the smallest area of the rolled workpiece, respectively. The $D_{min_{av}}$ is the average of 12 diameters uniformly distributed on the transverse section with the smallest area. The larger the RDR value, the more serious the necking defect in the rolled part.

Analysis of symmetrical central cross-sectional necking

The high temperature compressive stress–strain curves for carbon steel materials [27, 28] and alloy steel materials [29, 30] fit the power exponential hardening material model. The true stress–strain curves for the 45 steel are shown in Fig. 9. At lower strain rates ($\leq 1\text{ s}^{-1}$) the stress–strain curve shows a small decrease due to dynamic recrystallization and dynamic recovery. However, at higher strain rates, the hardening phenomenon appears that the stress remains constant or the stress increases gradually with the increase of strain. This means that as the strain increases the level of yield stress also increases. In the cross wedge rolling process, higher stress level and larger deformation are often required when the necking defect occurs. TC4 alloy is different from carbon steel materials and alloy steel materials, and it is very sensitive to thermal deformation parameters. The true stress–strain curves below the β phase transition temperature have obvious flow softening phenomenon. Due to the existence of softening, the stress decreases with increasing strain during the rolling process. Therefore, TC4 alloy is prone to necking defects during CWR.

If the CWR process parameters are improperly selected, the cross-section at the symmetric center of the rolled workpiece is prone to necking due to excessive axial tension. The slight necking defects can lead to increased machining allowance and reduced material utilisation, and the serious necking defects will cause the rolled workpiece to scrap. Therefore, it is necessary to analyze the influence of the broadening angle on the cross-sectional thinning of the

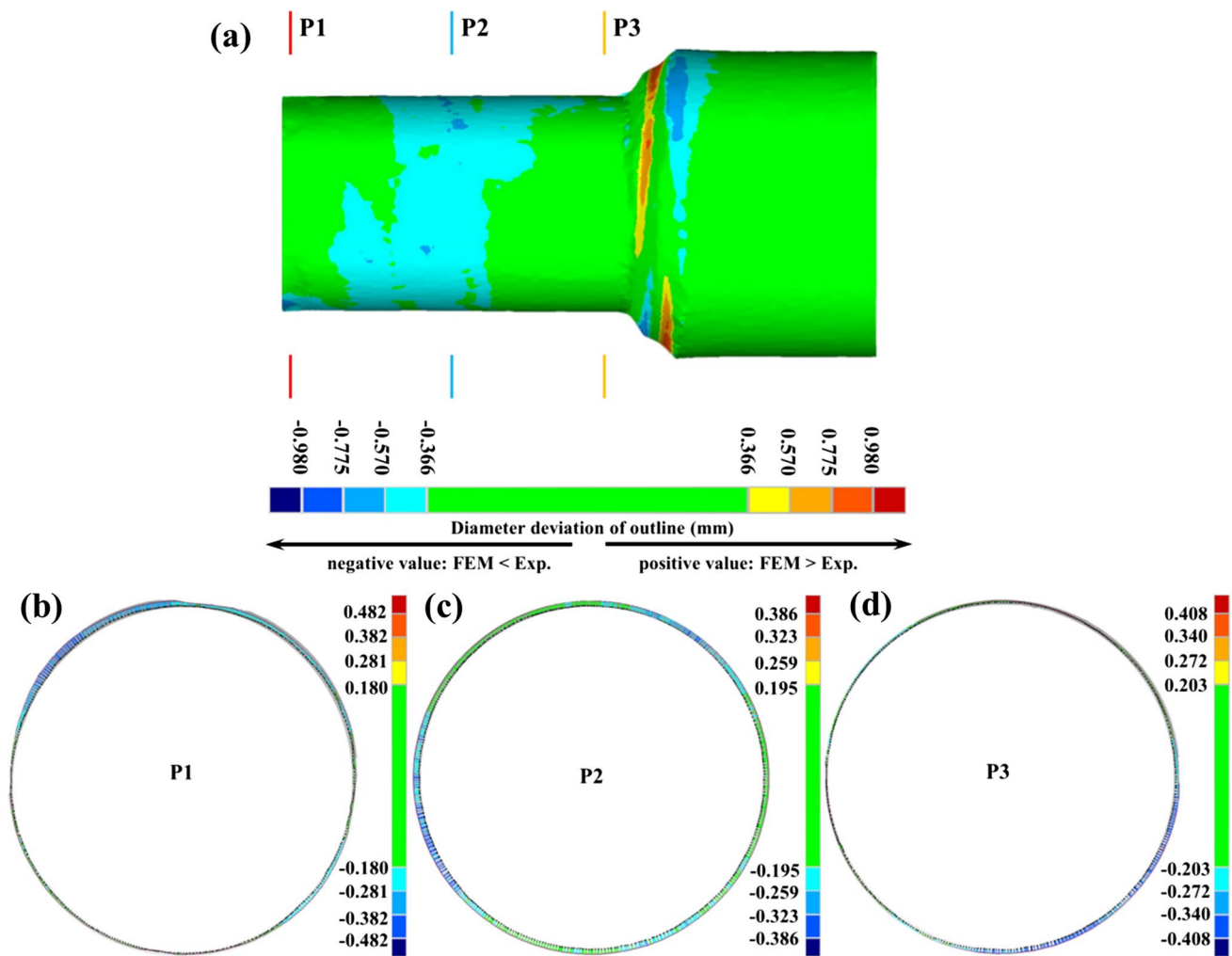


Fig. 8 Comparison of experimental and simulation results for the outline of the rolled part

symmetric center. Hu et al. [10] proposed a simple model for the CWR process without necking defects:

$$F_z < \frac{(\pi d^2 \rho)}{8 \sin \alpha} \tag{10}$$

where F_z is the axial force, d is the diameter of the workpiece after rolling, ρ is the yield stress, and α is the forming angle.

To clarify the influence of forming angle α and stretching angle β on the rolling stress to which the rolled workpiece is subjected and find the main cause of the necking defect. It is necessary to analyze the force condition provided by the wedge surface of the die to the rolled workpiece. The force diagram on the wedge surface of the die is shown in Fig. 10. The Z-axis direction is consistent with the axial direction of the rolled workpiece, and the XOY plane is parallel to the cross section of the rolled

workpiece. In Fig. 10a, the rolling force F is perpendicular to the bevel $klmn$ of the die. The force F can be decomposed into F_y along the Y direction and F_t in the XOZ plane. The force F_t is decomposed into forces F_x and F_z along the X and Z axes, respectively, as shown in Fig. 10b.

The component force of rolling force in the deformation zone is shown in Eqs. (11) to (13):

$$F_x = F \cdot \sin \alpha \cdot \sin \beta \tag{11}$$

$$F_y = F \cdot \cos \alpha \tag{12}$$

$$F_z = F \cdot \sin \alpha \cdot \cos \beta \tag{13}$$

It can be seen from Eq. (13) that when the forming angle α increases or the stretching angle β decreases, the F_z increases accordingly. The increase in axial force contributes to the creation of necking defects.

Fig. 9 True stress–strain curves of 45 steel [27]: **a** $T=1050\text{ }^\circ\text{C}$, **b** $T=1100\text{ }^\circ\text{C}$, **c** $T=1150\text{ }^\circ\text{C}$, **d** $T=1200\text{ }^\circ\text{C}$

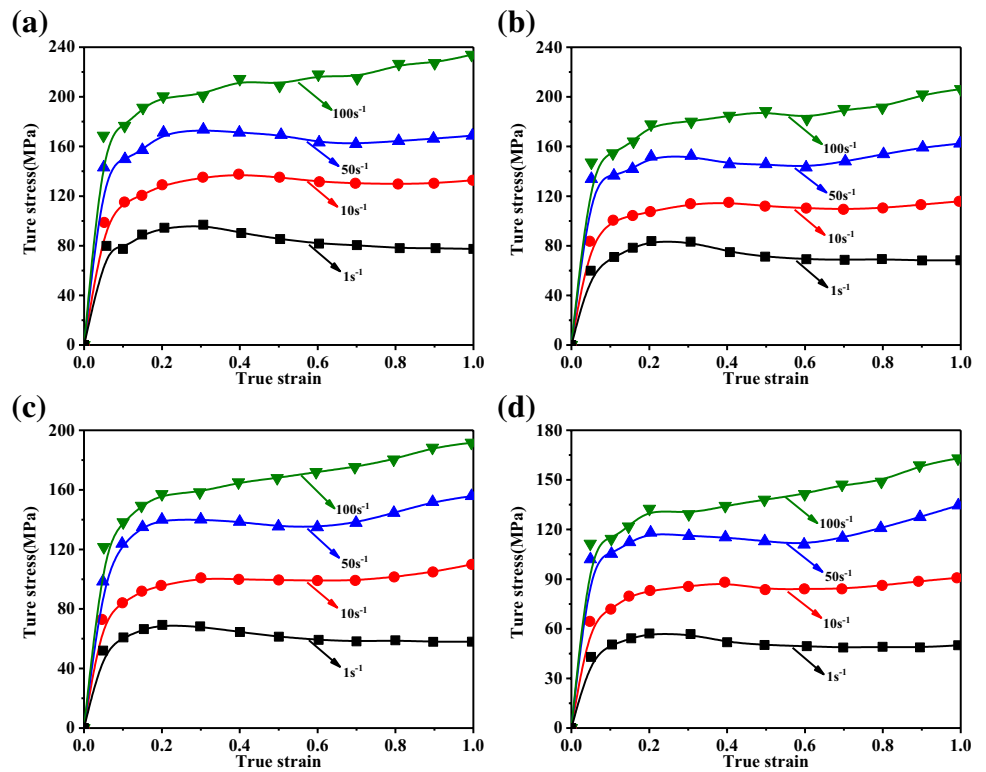
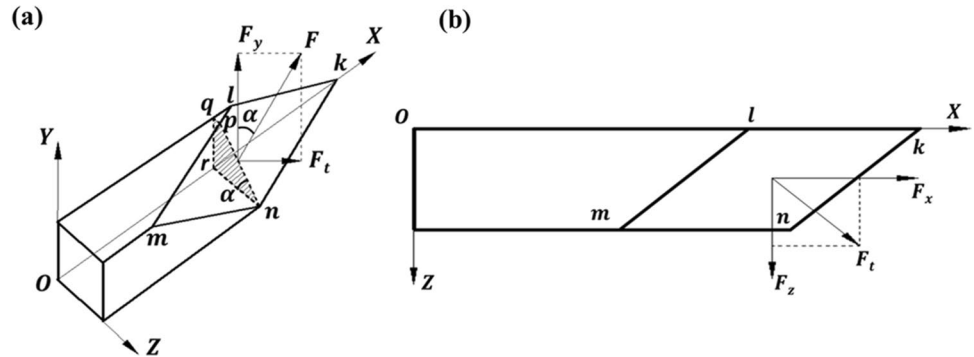


Fig. 10 Rolling force diagram in deformation zone: **a** space force diagram **b** component on XOZ plane



The effect of stretching angle

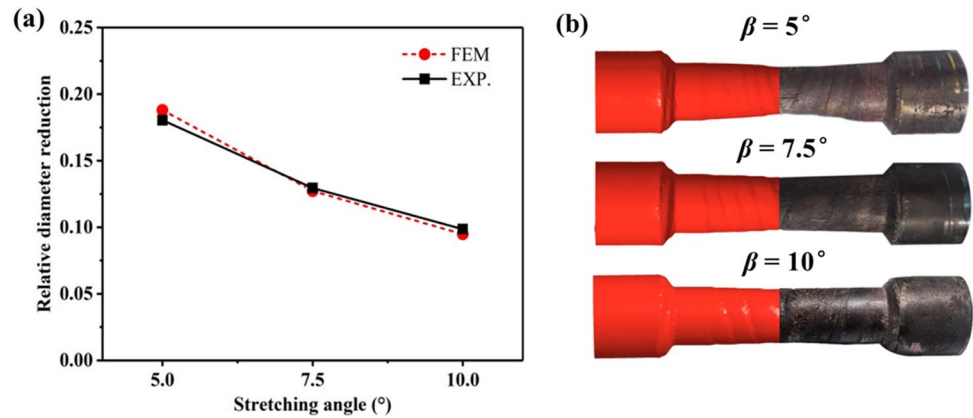
The effect of the stretching angle on the RDR of the rolled part for a forming angle of 30° , a deformation temperature of $870\text{ }^\circ\text{C}$ and an area reduction of 50% is shown in Fig. 11. In Fig. 11a FEM and EXP. are used to represent the simulation results of the finite element model and the experimental results, respectively. With the increase of the stretching angle, a significant decrease of the RDR appears. In Fig. 10b, the necking defect at the center of symmetry of the rolling part is significantly improved.

The peak and steady-state values of the axial force at different stretching angles in Fig. 12 decrease as the stretching angle increases. The axial force reaches its peak when the knifing stage is complete. Due to the softening effect of

TC4 alloy, the axial force decreased significantly after entering the stretching stage. In the sizing stage, the axial force decreases again due to the disappearance of the stretching effect.

The change in the strain at a point on the surface at the center of symmetry of the rolled part at different stretching angles is shown in Fig. 13. In Fig. 13b and c, the radial strain and circumferential strain are mainly compressive strain, and there is a small tensile strain at the beginning of rolling. The strain value increases gradually and reaches a stable value during the sizing process. The radial and circumferential strain values are maximum when the stretching angle is 5° . Axial strains are expressed as tensile strains during the rolling process. The smaller the tensile angle is, the larger the axial strain value is, which means that the metal flow

Fig. 11 Effect of stretching angle of the die on the relative diameter reduction: **a** relationship between the relative diameter reduction and stretching angle, **b** workpieces with different stretching angles



increases along the axial direction. In conclusion, at a small tensile angle, the increase in axial tensile strain and radial compressive strain of the metal promotes the increase in the RDR of the rolled part.

The effect of forming angle

The effect of the forming angle on the RDR of the rolled part for a stretching angle of 7.5° , a deformation temperature of 870°C and an area reduction of 50% is shown in Fig. 14. A small increase in RDR occurs as the forming angle increases.

The peak and steady-state values of the axial force in Fig. 15 gradually increase with the increases of the forming angle. At higher axial forces (i.e. $\alpha = 35^\circ$), the metal can be more easily "driven" in the axial direction to the sides of the rolled part. After entering the stretching stage, the axial force increases with the continuation of rolling, so the cross-sectional diameter of the symmetric center becomes smaller and smaller.

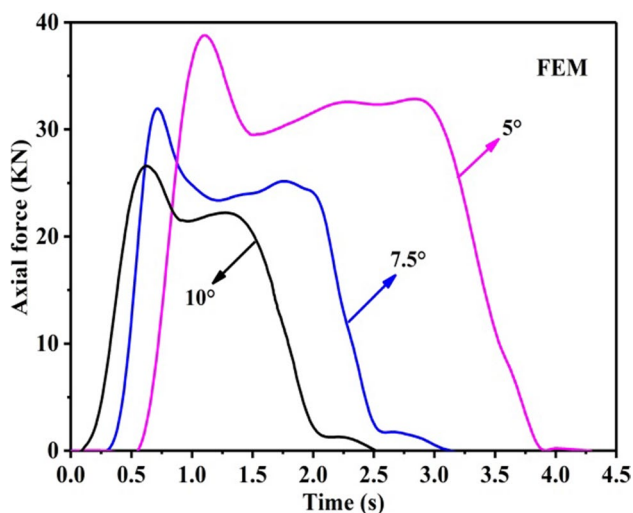


Fig. 12 Variation in axial force at different stretching angles

The change in the strain at a point on the surface at the center of symmetry of the rolled workpiece at different forming angles is shown in Fig. 16. In Fig. 16b and c, the radial strain and circumferential strain increase gradually and reach a constant value in the sizing stage. The two strains are mainly compressive strain, and there are obvious differences in the numerical value. When the forming angle is relatively large (i.e. $\alpha = 35^\circ$), both the radial and circumferential strains are greater than the strains at the other two forming angles. The axial strains in Fig. 16a are all tensile strains, and the larger forming angle corresponds to the larger axial strain. The above analysis shows that the elongation of the compressed metal along the axial direction increases continuously at a large forming angle, which makes the RDR of the rolled part increase.

The effect of deformation temperature

The effect of the deformation temperature on the RDR of the rolled part at a forming angle of 30° , a stretching angle of 7.5° , and an area reduction of 50% is shown in Fig. 17. As the deformation temperature increases, the RDR also shows a significant decrease. The value of the RDR at 910°C is close to 0, and the rolling zone has good forming quality.

As can be seen in Fig. 18a and b, the radial force results predicted by the FEMs are close to the experimental results. When the deformation temperature is 910°C and 850°C , the steady radial force is about 51 KN (53 KN in the experiment) and 74.5 KN (79 KN in the experiment), respectively. This shows that the FE results are reliable. According to Fig. 18, the steady radial force, torque and axial force gradually increase with the decrease of deformation temperature. This is due to the resistance to the flow of the material gradually increases as the deformation temperature decreases. With the increase in the axial force, the stress acting on the cross-section of the rolled workpiece increases, and the risk of necking defect increases.

The forming quality of the rolled workpiece is mainly affected by the law of material flow. According to the

Fig. 13 Strain variation at different stretching angles: **a** axial strain, **b** radial strain, **c** circumferential strain

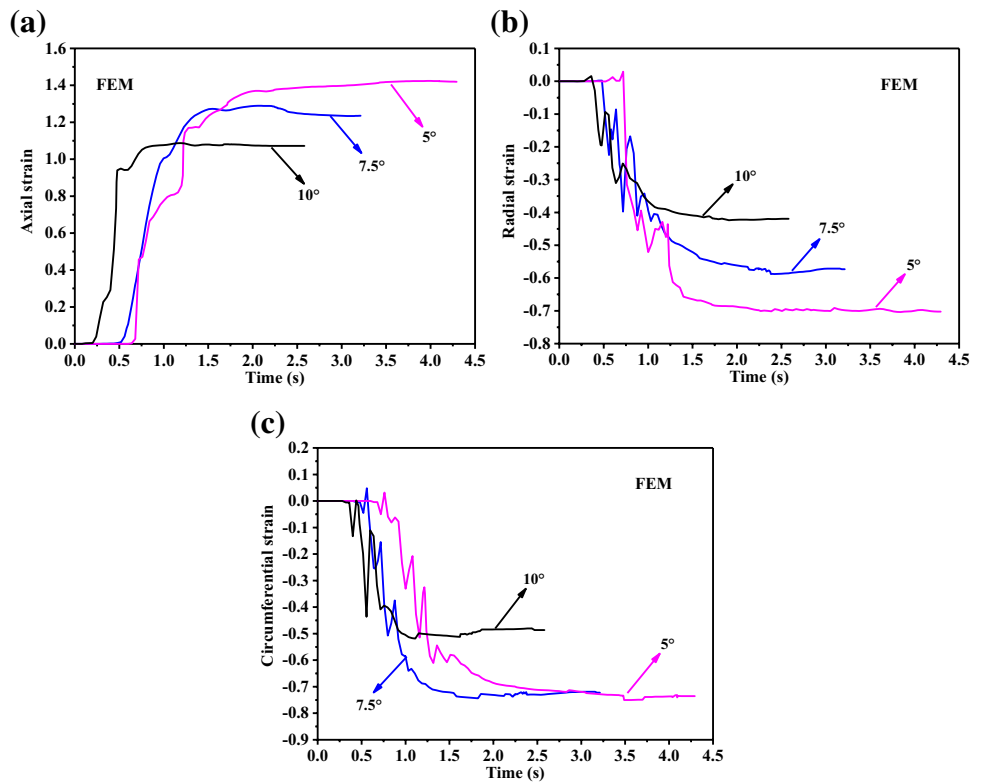
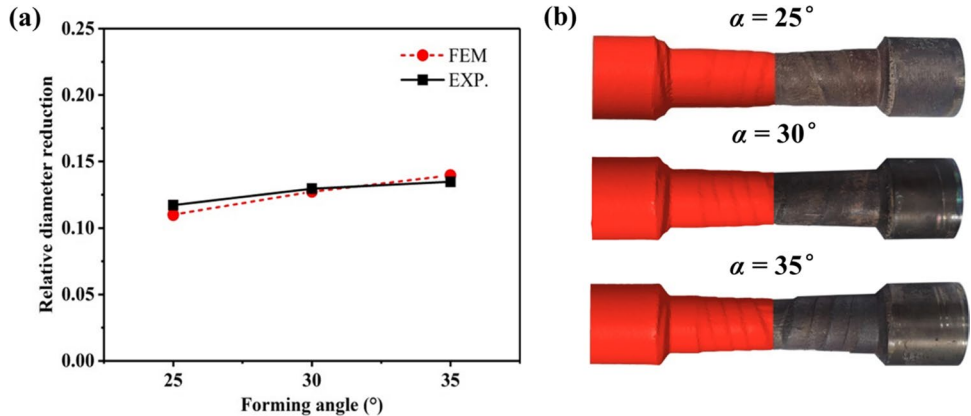


Fig. 14 Effect of forming angle of the die on the relative diameter reduction: **a** relationship between the relative diameter reduction and forming angle, **b** workpieces with different forming angles



variation of tracking points with equal spacing shown in Fig. 19, the influence of different deformation temperatures on the flow of TC4 alloy material was analyzed. In Fig. 19, the workpiece at $T = 850^\circ\text{C}$ is about to enter the sizing stage when $t = 1.98\text{ s}$, and these tracking points have moved in varying degrees.

The axial and radial displacement changes of the tracing points at different deformation temperatures when $t = 1.98\text{ s}$ are shown in Fig. 20. Comparing the axial displacement of tracking points at different deformation temperatures, it can be seen that the trend of the axial flow of tracking points is basically the same, and the axial displacement values close to the core are greater than that at the surface. The axial displacement values for the surface tracking points of the same

cross-section do not differ significantly. The displacement of the material at the core of the rolled workpiece along the axial direction increases with the decrease of deformation temperature. In Fig. 20e, the material near the symmetrical section flows in a radial direction from the surface to the core, resulting in the obvious necking phenomenon on the surface of the symmetric center position of the rolled workpiece. The axial displacement of the material at the core position decreases as the deformation temperature rises to 910°C . At the same time, the difference between the axial displacement of the material at the core and the surface becomes correspondingly small. This indicates a uniform axial movement of the material at each cross-sectional position of the rolled workpiece as the temperature increases.

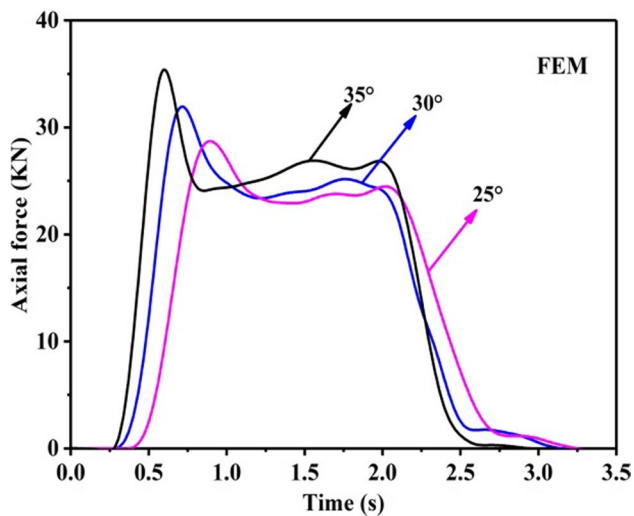
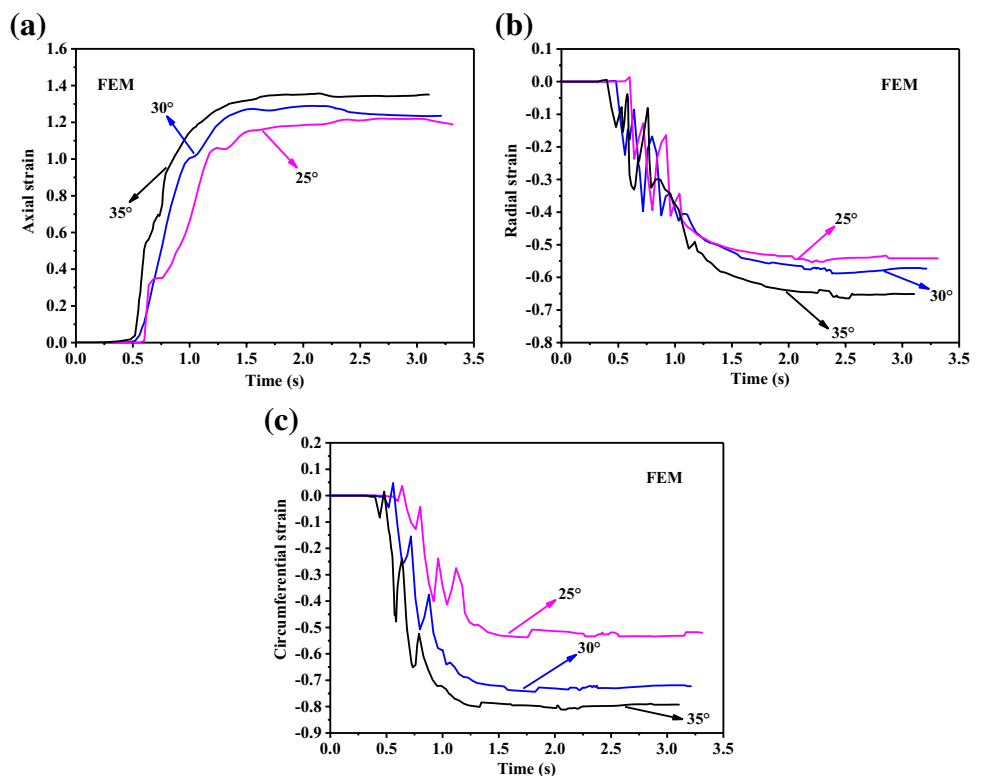


Fig. 15 Variation in axial force at different forming angles

At 910 °C, the material was more likely to flow in the circumferential direction in the closed cavity consisting of the dies and guide slats, and its tendency to flow in the radial direction was weakened. Therefore, the RDR value of the rolled part under this condition is close to 0. There is no necking defect on the surface of the rolled part. In the process of rolling TC4 alloy by CWR, appropriate deformation temperature should be selected to avoid necking defects due to too low deformation temperature.

Fig. 16 Strain variation at different forming angles: **a** axial strain **b** radial strain, **c** circumferential strain



The effect of area reduction

The effect of area reduction on the RDR of the rolled part at a forming angle of 30°, a stretching angle of 7.5° and a deformation temperature of 870 °C is shown in Fig. 21. The RDR is negative for area reduction in the range of 10–30%. A significant step appears in the middle of the two parts, which indicates that the diameter in the middle of the part is larger than the target diameter. When the area reduction increases to 50%, a necking defect appears in the middle of the rolled part. The RDR value increases sharply as the area reduction continues to increase to 70%.

The variation of the axial force for different area reduction is shown in Fig. 22. The axial forces tend to increase with increasing values of area reduction. When the area reduction is 70%, large deformation heat is generated, and the flow stress level of the metal is reduced. Simultaneously, with the development of plastic deformation, the softening effect of the metal is triggered. Therefore, the decrease of axial force value under the combined action of the above two factors is much larger than that of area reduction of 50%. In the later stage of the stretching stage, the axial force continues to increase, and the deformation was concentrated in the middle region of the rolled workpiece, resulting in serious necking.

The influence of area reduction on the contact area of rolled workpieces is shown in Fig. 23. The contact area consists of the arc area F1 and the spiral area F2, which are the

Fig. 17 Effect of deformation temperature on relative diameter reduction: **a** relationship between the relative diameter reduction and deformation temperature, **b** workpieces with different deformation temperatures

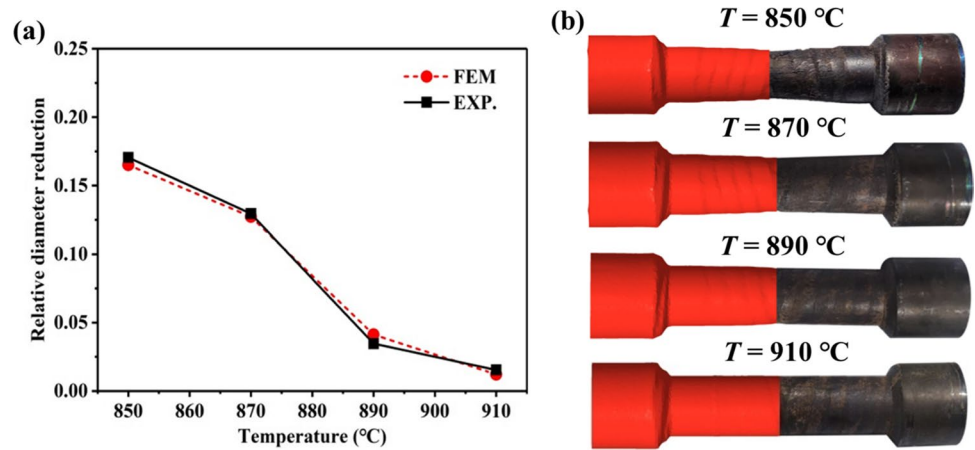
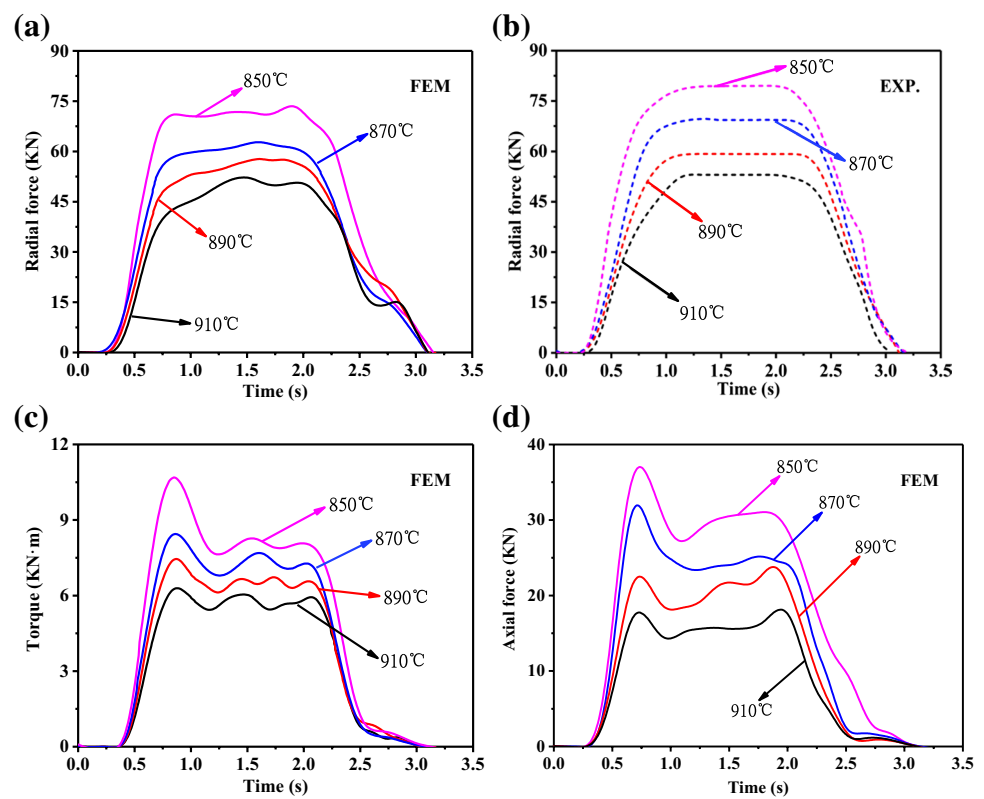


Fig. 18 Effectiveness of the deformation temperature on radial force, torque and axial force in CWR process: **a** FE simulation results of radial force, **b** experimental results of radial force, **c** FE simulation results of torque, **d** FE simulation results of axial force



contact between the top surface of the die and the workpiece, and the contact between the wedge surface of the die and the workpiece, respectively. Arc area F1 cannot increase the axial flow of metal. The force exerted on the rolled workpiece by spiral contact area F2 can be divided into radial force, tangential force and axial force. The metal is compressed by the radial force, and the compressed metal is easy to flow along the axial direction due to the axial force.

Changes in area reduction values can significantly change the area ratio of F2 to F1. In Fig. 23a and b, when the area reduction is 10% and 30% respectively, the area of contact surface F1 is much larger than that of F2. The metal flow in the tangential direction is greater than the

axial direction. Therefore, the cross-section of the rolling zone of the rolled workpiece is easy to form an ellipse, making the diameter larger than the target diameter. The metal enters the gap on the surface of the die and forms a step on the surface of the rolled workpiece. In Fig. 23c and d, the area of the contact surface F1 decreases continuously as the area reduction value increases, while the area of F2 increases. This results in a weakened flow of metal in the tangential direction and an improved flow in the axial direction. The RDR of the rolled part is increased by the combined effect of these two factors. Multi-pass rolling can be considered when rolling workpiece with a large area reduction.

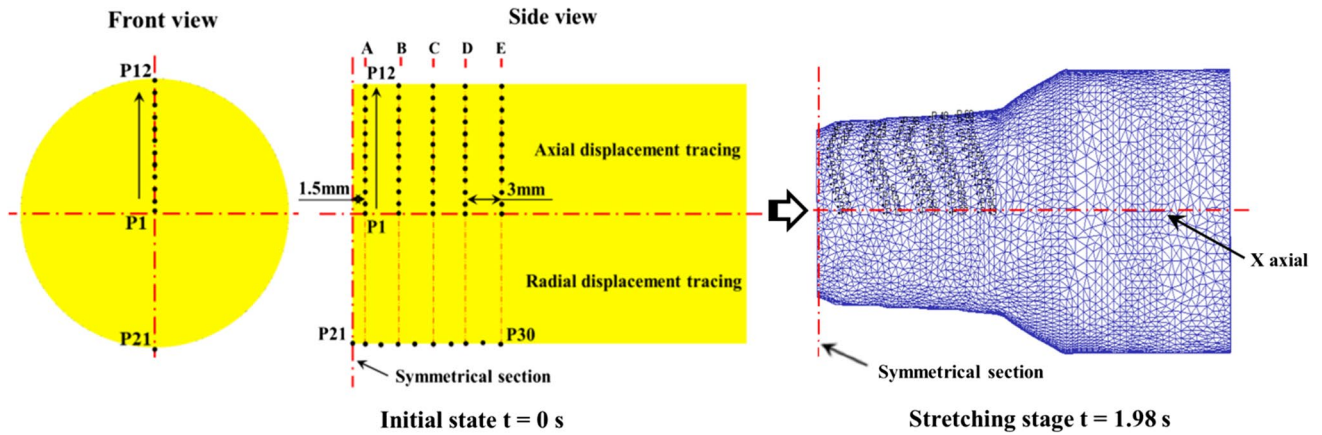


Fig. 19 the location of the tracing points

Fig. 20 The displacement along the axial and radial direction in the CWR process: **a** $T=850\text{ }^{\circ}\text{C}$, **b** $T=870\text{ }^{\circ}\text{C}$, **c** $T=890\text{ }^{\circ}\text{C}$, **d** $T=910\text{ }^{\circ}\text{C}$, **e** the radial displacement

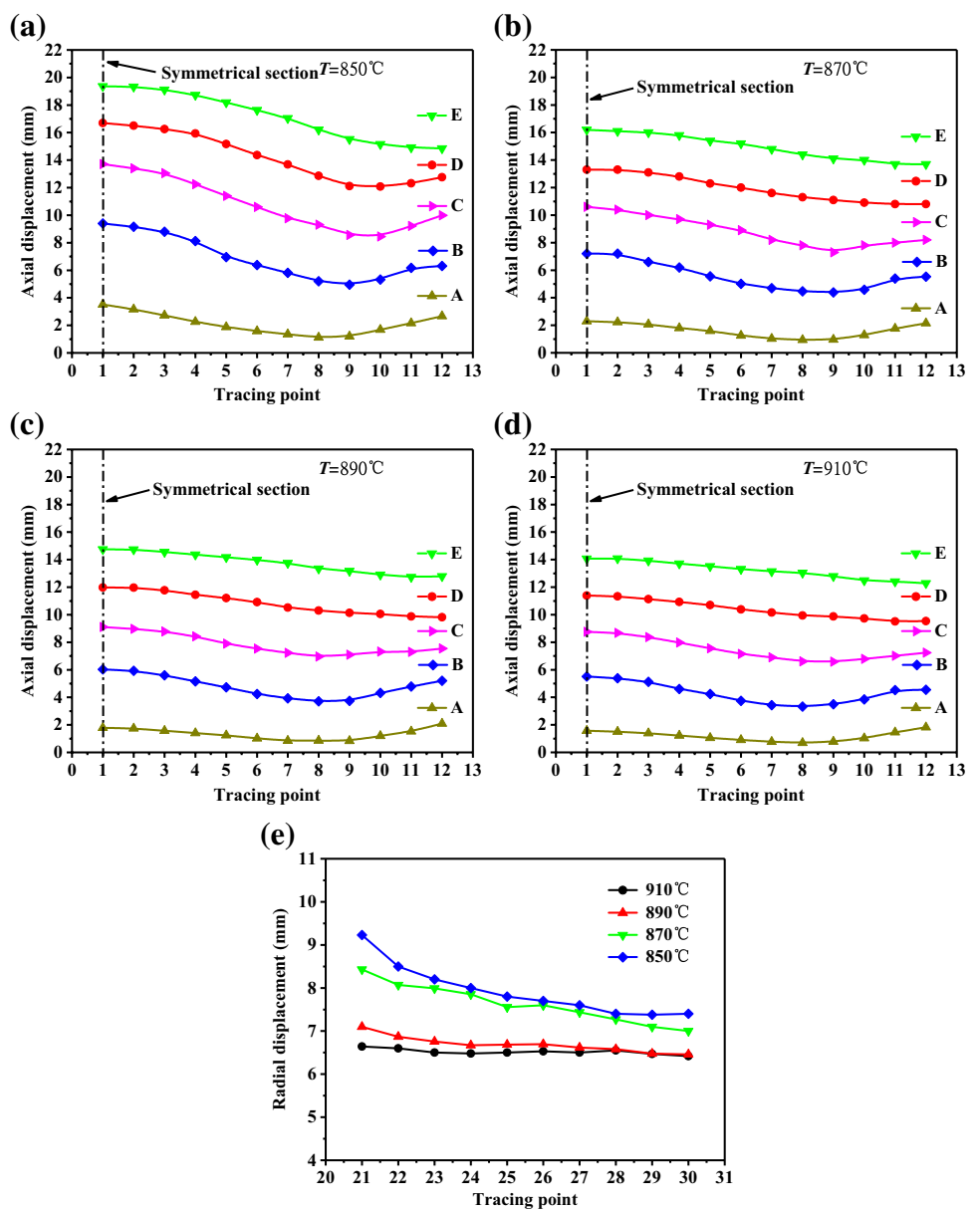


Fig. 21 Effect of area reduction on relative diameter reduction: **a** relationship between the relative diameter reduction and area reduction, **b** workpieces with different area reductions

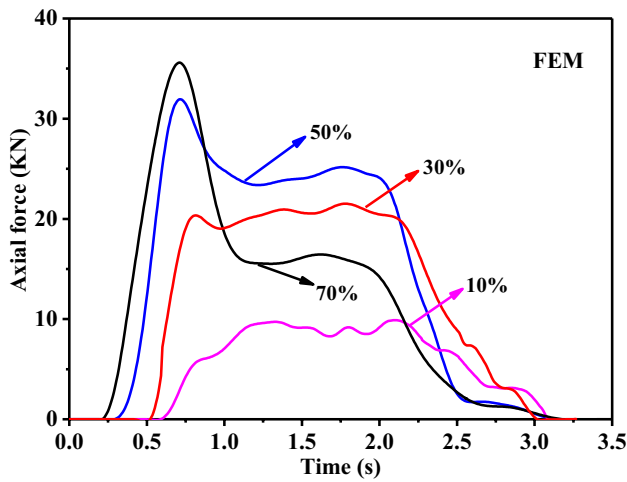
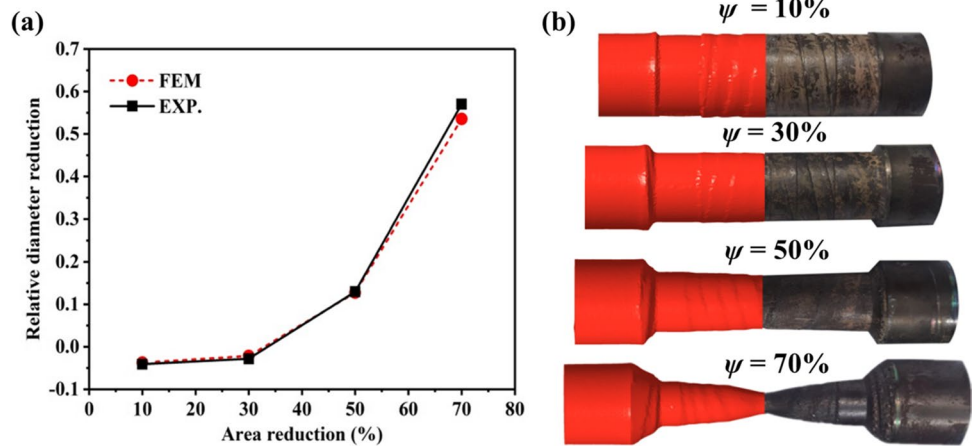


Fig. 22 Variation in axial force at different area reduction

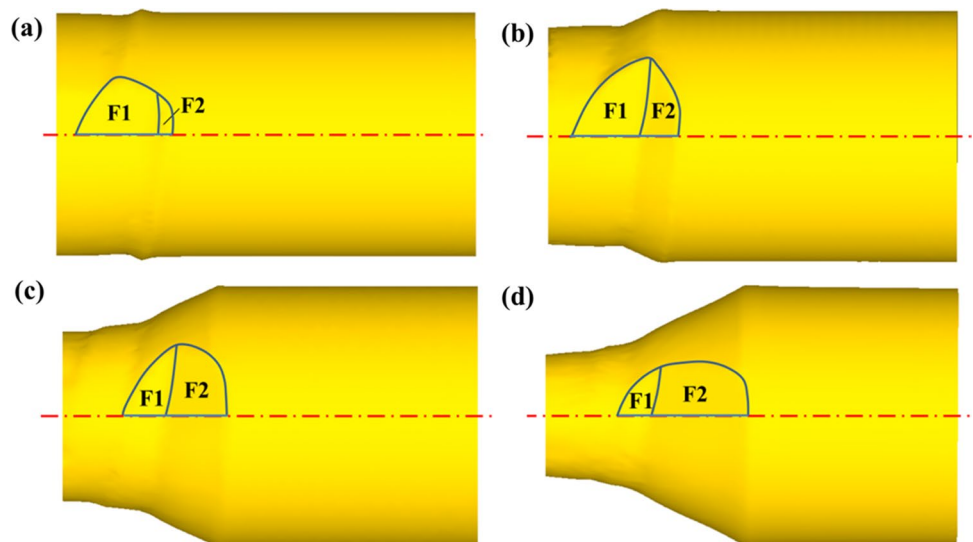
Mechanical properties and microstructure

The effect of deformation temperature

In the present study, the microstructure and the mechanical properties of rolled parts with deformation temperature of 850 °C, 870 °C, 890 °C and 910 °C, area reduction of 50% and after water cooling were compared and analyzed. The room temperature tensile sample was taken along the axial direction of the rolled parts, and its location is shown in Fig. 24. The ultimate tensile strength (UTS), yield strength (YS), and the elongation (El) of the TC4 alloy as-received at room temperature were 947 MPa, 873 MPa and 16.9%, respectively. The volume fraction of the primary α phase was measured using Image Pro-plus software.

The room temperature mechanical properties and content of the primary α phase at different deformation

Fig. 23 Contact area at different area reduction: **a** $\psi = 10\%$, **b** $\psi = 30\%$, **c** $\psi = 50\%$, **d** $\psi = 70\%$



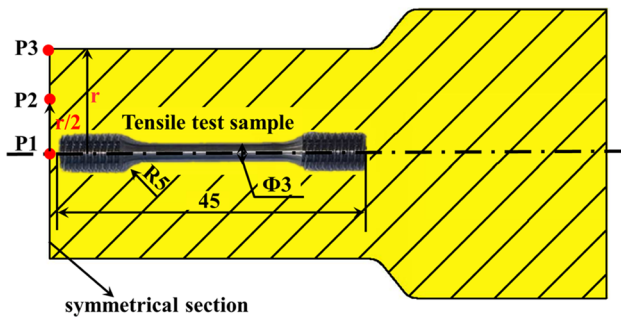


Fig. 24 Distribution of sampling location for tensile specimen and microstructure

temperatures are shown in Fig. 25. The UTS and YS values at these four deformation temperatures are higher than those at the as-received state. The UTS and YS values decrease with the increase of deformation temperature, while the EI value is the opposite. It can be seen from Fig. 25b that the distribution of the primary α phase is not uniform in the cross section of the rolled parts with deformation temperatures of 870 °C and 910 °C. Under the combined effect of temperature reduction caused by die cooling and air heat exchange and temperature rise caused by plastic deformation, the temperature distribution of the rolled part is not uniform. Therefore, the volume fraction distribution of α phase is not uniform. The trend of f_{α_e} from P1 to P3 is the same for different deformation temperatures. That is, the f_{α_e} value increases gradually from the center to the surface along the radial direction. When the deformation temperature decreases from 910 °C to 850 °C, the volume fraction of the primary α phase

gradually increases and the volume fraction of the β phase gradually decreases as the temperature decreases [21].

From Fig. 26a-h, it can be seen that the grains in the deformation zone appear to be refined due to rolling deformation, which makes UTS and YS increase at different temperatures. When the temperature rises to 910 °C the secondary α phase disappears. During the rolling process, the deformation at P3 is greater than at P2 and P1 because the effective stress and effective strain decrease gradually from the contact surface along the radial direction to the core [31], and the deformation of microstructure morphology is also decreasing. In Fig. 26a and b, the primary α phase at P3 is obviously distorted and refined, and a large number of recrystallized grains are produced. In the microstructure of Fig. 26c and e, many tiny needle-like secondary α phase can be observed. These secondary α phase act as α -clusters distributed on the β phase matrix, which makes cracks more likely to encounter obstacles in the diffusion process, resulting in the increase of UTS and YS of the material [15]. At a deformation temperature of 910 °C, the needle-like secondary α phase is transformed into β phase, and the number of grain boundaries is reduced, resulting in a decrease in the UTS and YS values of the material. In Fig. 26g, the f_{α_e} value reaches the maximum. A large number of equiaxed α grains can make the stress uniformly distributed around the grains, and the strength properties of the material were further improved by the interweaving of the equiaxed α phase with the disordered secondary α phase. The disordered secondary α phase weakens the plasticity of the material.

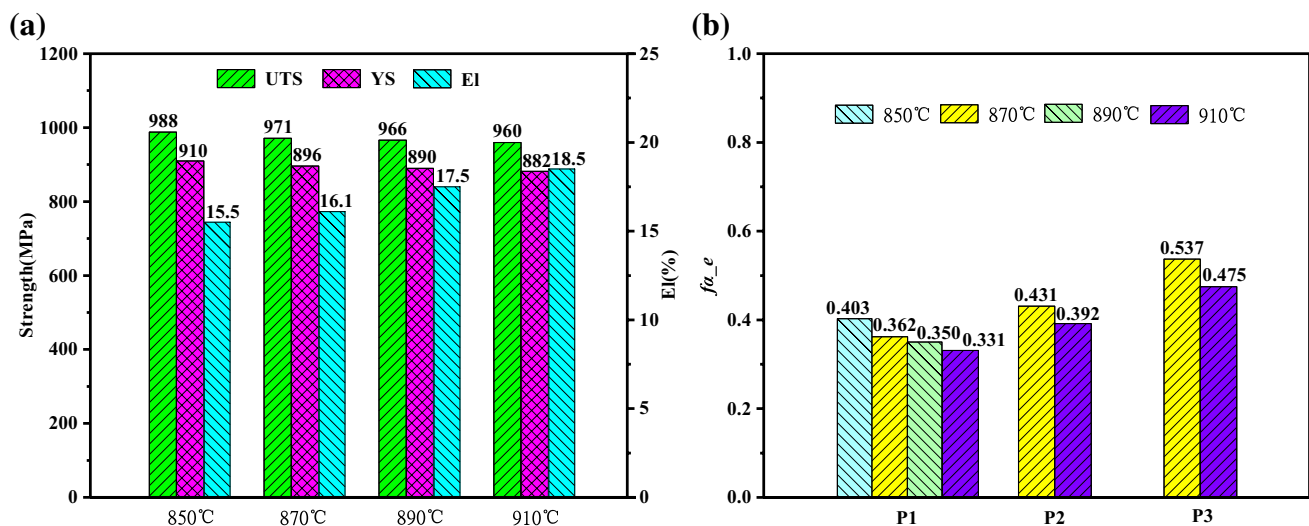
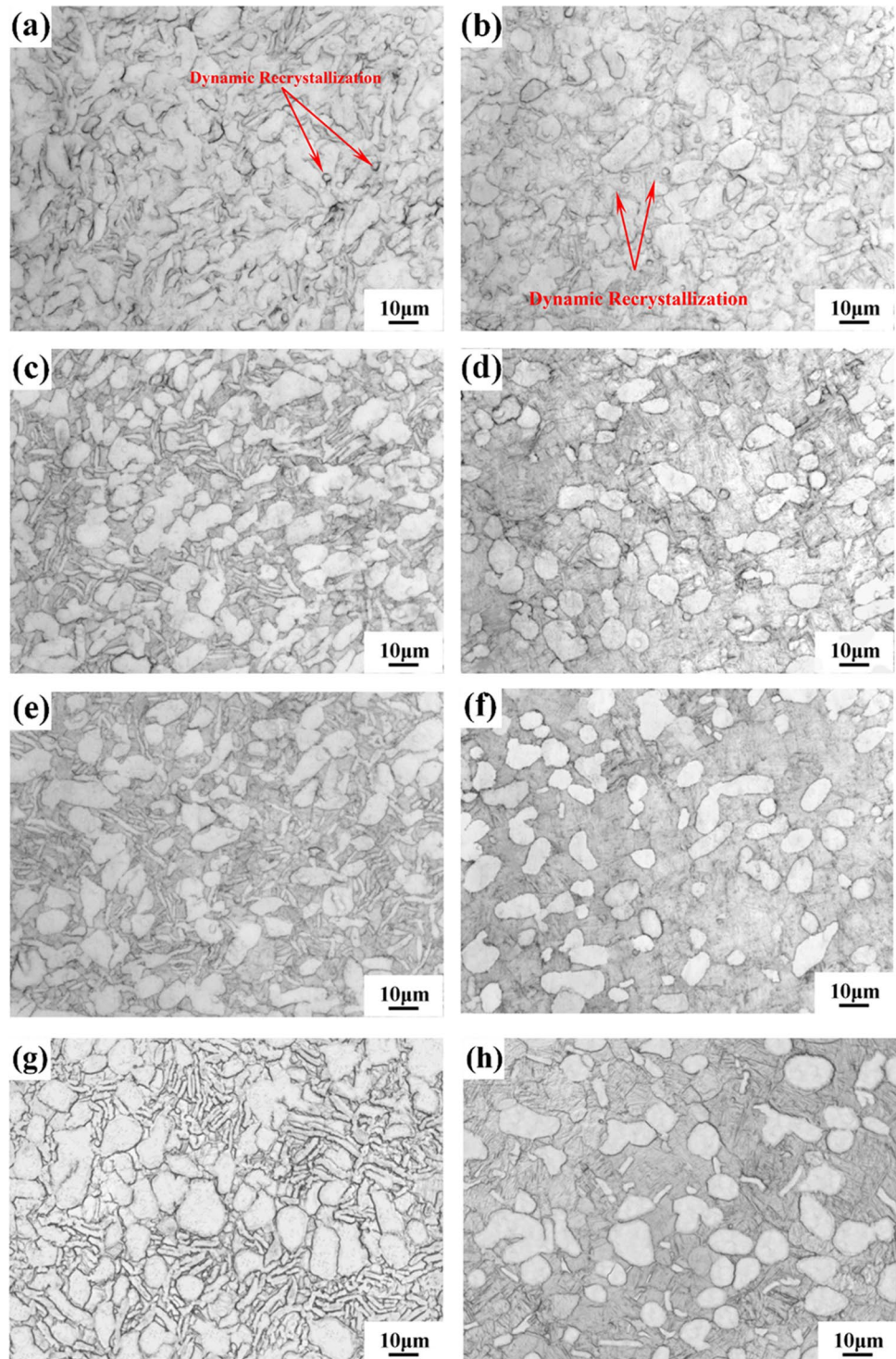


Fig. 25 a Mechanical properties and b content of the primary α phase of TC4 alloy shafts at different deformation temperatures

Fig. 26 The microstructure distribution of rolled parts at different deformation temperatures: **a** $T=870\text{ }^{\circ}\text{C}$, P3; **b** $T=910\text{ }^{\circ}\text{C}$, P3; **c** $T=870\text{ }^{\circ}\text{C}$, P2; **d** $T=910\text{ }^{\circ}\text{C}$, P2; **e** $T=870\text{ }^{\circ}\text{C}$, P1; **f** $T=910\text{ }^{\circ}\text{C}$, P1; **g** $T=850\text{ }^{\circ}\text{C}$, P1; **h** $T=890\text{ }^{\circ}\text{C}$, P1



The effect of stretching angle and forming angle

The effect of different stretching and forming angles on the mechanical properties and microstructure at an area reduction of 50% and a deformation temperature of $870\text{ }^{\circ}\text{C}$ are shown in Figs. 27 and 28. As can be seen from Fig. 27a, the changes of UTS, YS and El of the samples are very small.

This means that the stretching angle and forming angle of the die did not have a significant effect on the mechanical properties of the rolled part. There is no significant difference in the f_{α_e} value as well as the α grain size in Fig. 28a-e. The thickness of the secondary α phase is also essentially the same. This indicates that the stretching and forming angles did not have a significant effect on the heat exchange

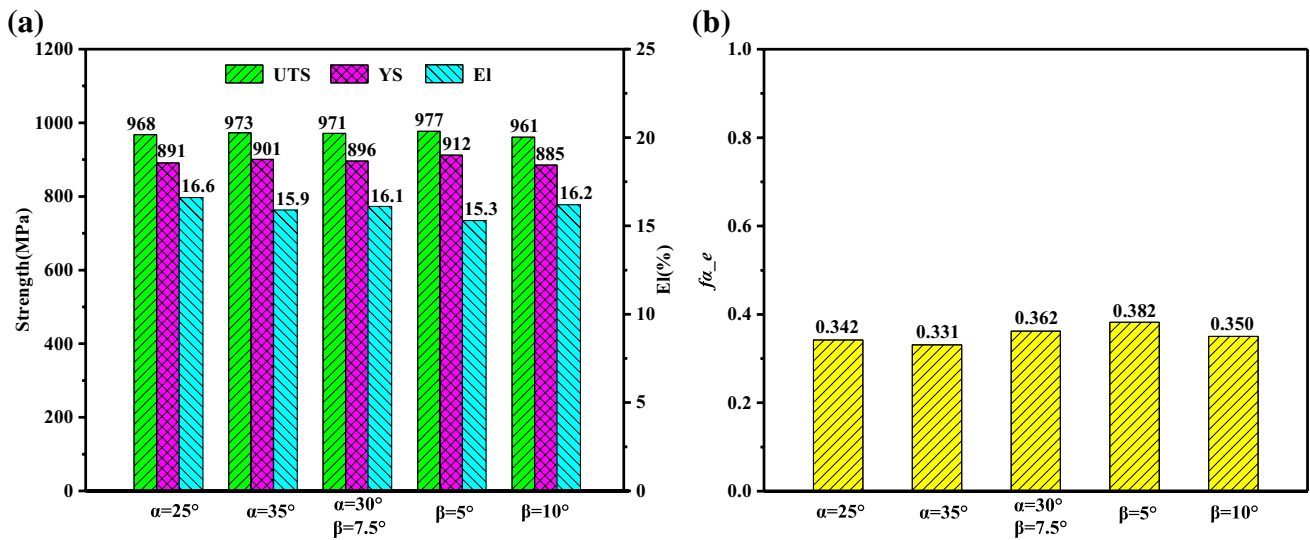
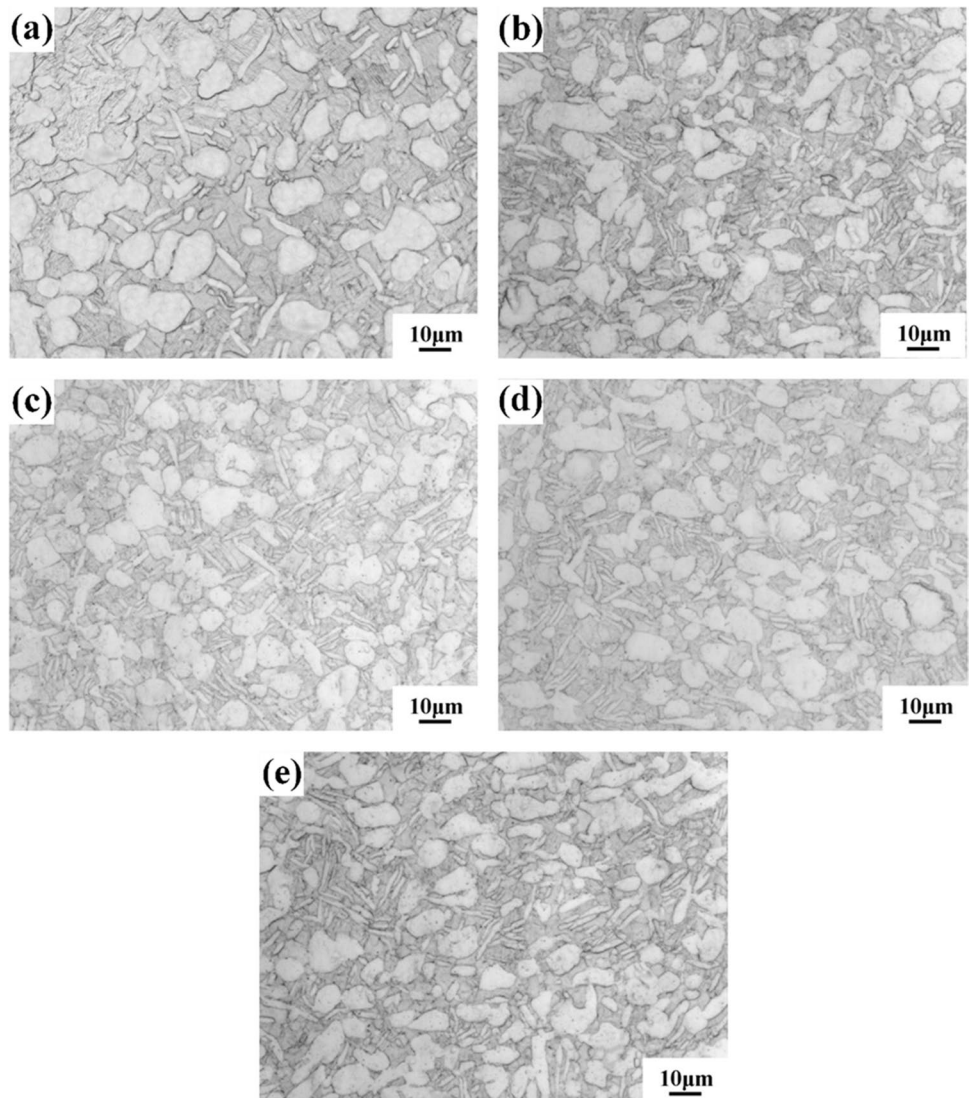


Fig. 27 a Mechanical properties and b content of the primary α phase of TC4 alloy shafts at different forming and stretching angles

Fig. 28 Effect of forming angle and stretching angle on micro-structure: **a** $\alpha = 25^\circ, \beta = 7.5^\circ, P1$; **b** $\alpha = 30^\circ, \beta = 7.5^\circ, P1$; **c** $\alpha = 35^\circ, \beta = 7.5^\circ, P1$; **d** $\alpha = 30^\circ, \beta = 5^\circ, P1$; **e** $\alpha = 30^\circ, \beta = 10^\circ, P1$



mechanism during CWR. The dies with different stretching and forming angles made the temperature changes of the rolled workpieces basically the same in the rolling process.

The effect of area reduction

The effect of different area reductions on the mechanical properties and the microstructure at a deformation temperature of 870 °C, a forming angle of 30° and a stretching angle of 7.5° are shown in Figs. 29 and 30. When the area

reduction is in the range of 10–30%, the strength level of the sample is relatively low. The primary α grain size is obviously larger, and the secondary α phase is coarse and parallel lamellar. This impairs the strength properties of the material. The orderly independent lamellar α phase can reduce the slip resistance and improve the plasticity. The $f_{\alpha-e}$ value shows no obvious change in this range. As the area reduction increases, the dislocation density increases and the primary α grain and secondary α grain size gradually decreases, which results in an increase in the strength

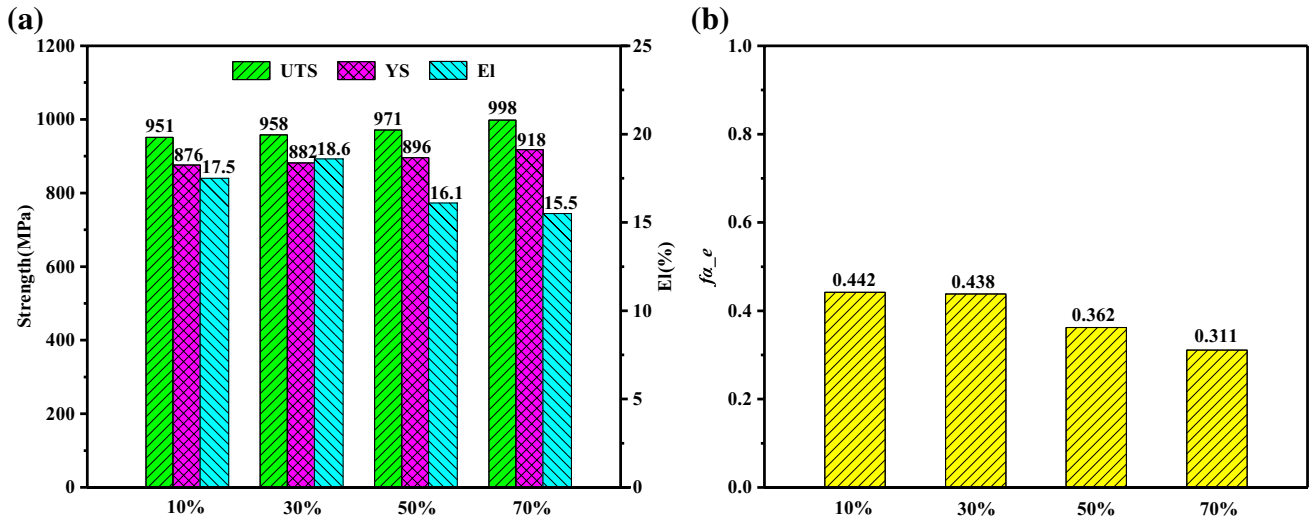
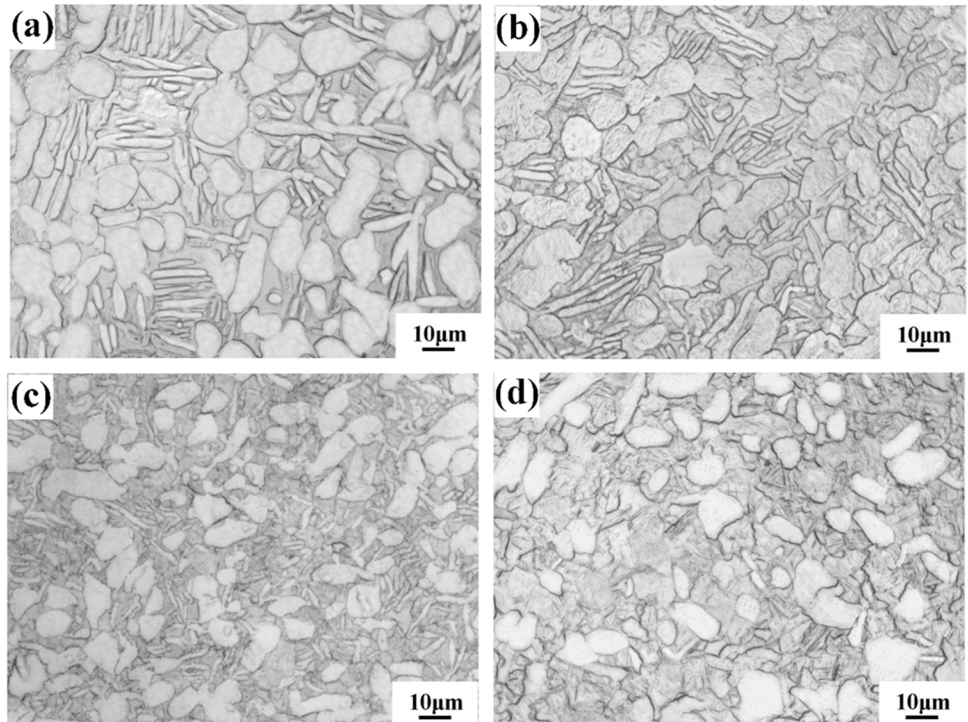


Fig. 29 a Mechanical properties and b content of the primary α phase of TC4 alloy shafts at different area reductions

Fig. 30 Effect of area reduction on microstructure: a $\psi=10\%$, P1; b $\psi=30\%$, P1; c $\psi=50\%$, P1; d $\psi=70\%$, P1



properties of the material. With the increase in area reduction, the plastic temperature rise increases, which promotes the transformation of α phase to β phase. The f_{α_e} value showed a downward trend. When the area reduction increases to 70%, the primary α grain size is further reduced, the volume fraction of the secondary α phase is significantly reduced, and the microstructure becomes uniform. This is because the increase in dislocation density and the increase in temperature provide sufficient driving force for dynamic recrystallization to occur, which reduces grain size.

Conclusions

In this paper, the CWR process of TC4 alloy was studied. The constitutive equation for the two-phase region was developed and applied to the FEM. The necking defects, metal flow, temperature distribution and force conditions of TC4 alloy can be accurately predicted by the model. The detailed conclusions are:

1. The constitutive equation of $\alpha + \beta$ region can effectively predict the flow stress of all deformation parameters with RR and $ARRE$ of 0.9982 and 5.67%, respectively. The equation is reliable for FEM.
2. Due to the obvious softening of the stress–strain curve, TC4 alloy is prone to necking defects during CWR below 950 °C. The occurrence of necking defects is also affected by axial force and metal flow. Increasing the stretching angle or decreasing the forming angle can reduce the axial force on the rolled workpiece. Increasing the deformation temperature, the flow of metal in the circumferential direction is enhanced, and the flow in the axial direction is weakened. The RDR value of the rolled workpiece will decrease under the above conditions. As the area reduction increases, the necking defects become serious. This is because the axial force and the contact area F_2 increase, and the flow of metal in the axial direction also increases. The use of Multi-pass rolling can avoid necking defects at large area reduction.
3. The heat exchange mechanisms at the surface and core of the rolling zone were different. Thus, the f_{α_e} value was distributed in a gradient, and gradually increasing from the core to the surface of the rolled parts. The interweaving of the equiaxed α phase with the disordered secondary α phase at lower deformation temperatures further improved the strength properties of the TC4 alloy. The disordered secondary α phase weakened the plasticity of the material.
4. The stretching and forming angle did not change the heat exchange mechanism of the rolled workpiece, and the f_{α_e} value and morphology did not change much. Consequently, the mechanical properties change little. By increasing the area reduction, the grain refinement and microstructure uniformity increased, and the dislocation density of the rolled workpiece also increased, which improved the strength properties of the rolled parts.
5. The mechanical properties and microstructure of the TC4 alloy can be improved by CWR. The comprehensive properties of the TC4 alloy parts were improved at the deformation temperatures of 890 to 910 °C. The minimum limit of area reduction should not be less than 30% to allow for grain refinement and improved strength properties.

Author contribution Peiai Li: conceptualization, investigation, methodology, data curation, writing-original draft, reviewing and editing.

Baoyu Wang: supervision, conceptualization, methodology, funding acquisition, reviewing and editing.

Cuiping Yang: supervision, methodology, reviewing and editing.

Huibo Zhang: supervision, methodology, reviewing and editing.

Wei Li: supervision, methodology, reviewing and editing.

Jing Zhou: supervision, methodology, reviewing and editing.

Funding This work is supported by the National Key R&D Program of China (Grant No. 2018YFB1307900), and the National Natural Science Foundation of China (Grant No. 51875036).

Data availability The datasets and material generated and/or analysed during the current study are available from the corresponding author on reasonable request.

Declarations

Conflicts of interest/Competing interests The authors have no conflicts of interest/competing interests to declare that are relevant to the content of this article.

Ethics approval The article follows the guidelines of the Committee on Publication Ethics (COPE) and involves no studies on human or animal subjects.

Consent to participate Applicable.

Consent to publish Applicable.

References

1. Feng PN, Yang CP, Wang BY, Li JL, Shen JX, Yang XM (2021) Formability and microstructure of TC4 titanium alloy hollow shafts formed by cross-wedge rolling with a mandrel. *Int J Adv Manuf Tech* 114(1–2):365–377. <https://doi.org/10.1007/s00170-021-06635-0>
2. Zbigniew P, Tomasz B, Janusz T (2016) Cross-wedge rolling of driving shaft from titanium alloy Ti6Al4V. *Key Eng Mater* 687(1):125–132. <https://doi.org/10.4028/www.scientific.net/KEM.687.125>
3. Arrazola PJ, Garay A, Lriarte LM, Armendia M, Marya S, Mañtre FL (2009) Machinability of titanium alloys (Ti6Al4V and

- Ti555.3). *J Mater Process Tech* 209(5):2223–2230 <https://doi.org/10.1016/j.jmatprotec.2008.06.020>
4. Guo P, Zhao YQ, Zeng WD, Hong Q. The effect of microstructure on the mechanical properties of TC4-DT titanium alloys (2013) *Mater Sci Eng A* 563(563):106–111 <https://doi.org/10.1016/j.msea.2012.11.033>
 5. Li JL, Wang BY, Fang S, Chen P (2020) A new process chain combining cross-wedge rolling and isothermal forging for the forming of titanium alloy turbine blades. *Int J Adv Manuf Tech* 108(5–6):1827–1838. <https://doi.org/10.1007/s00170-020-05451-2>
 6. Hu ZH, Zhang KS, Wang BY, Shu XD, Yang CP (2004) Forming technology and simulation of cross wedge rolling parts. Metall Ind Press, Beijing (**in Chinese**)
 7. Ji HC, Liu JP, Wang BY, Zheng ZH, Huang JH, Hu ZH (2015) Cross-wedge rolling of a 4Cr9Si2 hollow valve: explorative experiment and finite element simulation. *Int J Adv Manuf Tech* 77(1–4):15–26. <https://doi.org/10.1007/s00170-014-6363-9>
 8. Ji HC, Liu JP, Wang BY, Zhang ZR, Zhang T, Hu ZH (2015) Numerical analysis and experiment on cross wedge rolling and forging for engine valves. *J Mater Process Tech* 221:233–242. <https://doi.org/10.1016/j.jmatprotec.2015.02.007>
 9. Li Q, Lovell MR, Slaughter W, Tagavi K (2002) Investigation of the morphology of internal defects in cross wedge rolling. *J Mater Process Tech* 125–126(3):248–257. [https://doi.org/10.1016/S0924-0136\(02\)00303-5](https://doi.org/10.1016/S0924-0136(02)00303-5)
 10. Hu ZH, Zhang KS, Wang BY, Shu XD, Yang CP (2004) Cross wedge rolling theory and application. Metall Ind Press, Beijing (**in Chinese**)
 11. Jia Z, Zhou J, Ji JJ, Lei ZZ, Xiang D, Sun XT (2013) Influence analysis of area reduction for necking in twice-stage cross wedge rolling. *Int J Adv Manuf Tech* 66(9–12):1407–1413. <https://doi.org/10.1007/s00170-012-4418-3>
 12. Pater Z (2006) Finite element analysis of cross wedge rolling. *J Mater Process Tech* 173(2):201–208. <https://doi.org/10.1016/j.jmatprotec.2005.11.027>
 13. Li JL, Wang BY, Ji HC, Huang X, Tang XF, Ma WP (2017) Effects of the cross-wedge rolling parameters on the formability of Ti-6Al-4V alloy. *Int J Adv Manuf Tech* 92(5–8):2217–2229. <https://doi.org/10.1007/s00170-017-0263-8>
 14. Shi ZF, Guo HZ, Liu R, Wang XC, Yao ZK (2015) Microstructure and mechanical properties of TC21 titanium alloy by near-isothermal forging. *Trans Nonferrous Met Soc* 25(1):72–79. [https://doi.org/10.1016/S1003-6326\(15\)63580-4](https://doi.org/10.1016/S1003-6326(15)63580-4)
 15. Zhai DJ, Shui Y, Yuan M, Zhang YY, He YB (2019) Effects of content and morphology of α phase on microstructure and mechanical properties of TC4 alloy. *Heat Treat Met* 44(10):129–34 <https://doi.org/10.13251/j.issn.0254-6051.2019.10.027> (**in Chinese**)
 16. Qin DY, Guo DZ, Zheng L, Li YL (2018) Dynamic recrystallization of Ti-5553 alloy during sub-transus thermomechanical processing: mechanisms and its role in formation of a bi-modal structure. *J Alloy Compd* 769:725–731. <https://doi.org/10.1016/j.jallcom.2018.08.053>
 17. Julien R, Velay V, Vidal V, Dahan Y, Forestier R (2018) Characterization and modeling of forged Ti-6Al-4V Titanium alloy with microstructural considerations during quenching process. *Int J Mech Sci* 142–143:456–467. <https://doi.org/10.1016/j.ijmecsci.2018.05.023>
 18. Xu JW, Zeng WD, Sun X, Jia ZQ (2015) Microstructure evolution during isothermal forging and subsequent heat treatment of Ti-17 alloy with a lamellar colony structure. *J Alloy Compd* 637:449–455. <https://doi.org/10.1016/j.jallcom.2015.03.042>
 19. Zhang ZX, Qu SJ, Feng AH, Hu X, Shen J (2019) Microstructural mechanisms during multidirectional isothermal forging of as-cast Ti-6Al-4V alloy with an initial lamellar microstructure. *J Alloy Compd* 773:277–287. <https://doi.org/10.1016/j.jallcom.2018.09.220>
 20. Huo YM, Lin JG, Bai Q, Wang BY, Tang XF, Ji HC (2017) Prediction of microstructure and ductile damage of a high-speed railway axle steel during cross wedge rolling. *J Mater Process Technol* 239:359–369. <https://doi.org/10.1016/j.jmatprotec.2016.09.001>
 21. Li JL, Wang BY, Qin Y, Fang S, Huang X, Chen P (2019) Investigating the effects of process parameters on the cross wedge rolling of TC6 alloy based on temperature and strain rate sensitivities. *Int J Adv Manuf Tech* 103(5–8):2563–2577. <https://doi.org/10.1007/s00170-019-03461-3>
 22. Feng PN, Yang CP, Wang BY, Li JL, Liu RE (2021) Microstructure and mechanical properties of TC4 titanium alloy hollow shaft formed by cross wedge rolling. *Archiv Civ Mech Eng* 21(3):1–15. <https://doi.org/10.1007/s43452-021-00276-6>
 23. Xu X, Dong LM, Ba HB, Zhang ZQ, Yang R (2016) Hot deformation behavior and microstructural evolution of beta C titanium alloy in β phase field. *Trans Nonferrous Met Soc* 26(11):2874–2882. [https://doi.org/10.1016/S1003-6326\(16\)64416-3](https://doi.org/10.1016/S1003-6326(16)64416-3)
 24. Li MQ, Li H, Luo J (2016) Precision forging of titanium. Sci Press, Beijing (**in Chinese**)
 25. Ning YQ, Xie BC, Liang HQ, Li H, Yang XM, Guo HZ (2015) Dynamic softening behavior of TC18 titanium alloy during hot deformation. *Mater Des* 71:68–77 <https://doi.org/10.1016/j.matdes.2015.01.009>
 26. Alabort E, Putman D, Reed RC (2015) Superplasticity in Ti-6Al-4V: Characterisation, modelling and applications. *Acta Mater* 95:428–442. <https://doi.org/10.1016/j.actamat.2015.04.056>
 27. Tao XG, Xu CG, Liu GH (2011) The determination of Zener-Hollomon parameter in ductile damage criteria. *J Plast Eng* 18(1):76–80. [https://doi.org/10.3969/j.issn.1007-2012.2011.01.016\(inChinese\)](https://doi.org/10.3969/j.issn.1007-2012.2011.01.016(inChinese))
 28. Bai M, Zhang C, Shen GB (2014) Stress-Strain Constitutive Model for Hot Deformation of 20A Steel. *J Net Form Eng* 6(4):52–57. [https://doi.org/10.3969/j.issn.1674-6457.2014.04.010\(inChinese\)](https://doi.org/10.3969/j.issn.1674-6457.2014.04.010(inChinese))
 29. Huang X, Wang BY, Mu YH, Shen JX, Li JL, Zhou J (2019) Investigation on the effect of mandrels on hollow shafts in cross-wedge rolling. *Int J Adv Manuf Tech* 102(1–4):443–455. <https://doi.org/10.1007/s00170-018-3093-4>
 30. Shen JX, Wang BY, Yang CP, Zhou J, Cao XQ (2021) Theoretical study and prediction of the inner hole reduction and critical mandrel diameter in cross wedge rolling of hollow shaft. *J Mater Process Technol* 294:117140. <https://doi.org/10.1016/j.jmatprotec.2021.117140>
 31. Li PA, Wang BY, Feng PN, Shen JX, Wang JP (2022) Numerical and experimental study on the hot cross wedge rolling of Ti-6Al-4V vehicle lower arm preform. *Int J Adv Manuf Tech* 118(9–10):3283–3301. <https://doi.org/10.1007/s00170-021-07979-3>

Publisher's Note Springer Nature remains neutral with regard to jurisdictional claims in published maps and institutional affiliations.

Springer Nature or its licensor holds exclusive rights to this article under a publishing agreement with the author(s) or other rightsholder(s); author self-archiving of the accepted manuscript version of this article is solely governed by the terms of such publishing agreement and applicable law.